ACS NANO

www.acsnano.org

ARTICLE

Targeting Senescent Alveolar Epithelial Cells Using Engineered Mesenchymal Stem Cell-Derived Extracellular Vesicles To Treat Pulmonary Fibrosis

Yaoying Long,[▽] Bianlei Yang,[▽] Qian Lei, Fei Gao, Li Chen, Wenlan Chen, Siyi Chen, Wenxiang Ren, Yulin Cao, Liuyue Xu, Di Wu, Jiao Qu, He Li, Yali Yu, Anyuan Zhang, Shan Wang, Weiqun Chen, Hongxiang Wang, Ting Chen, Zhichao Chen,* and Qiubai Li*

Cite This: *ACS Nano* 2024, 18, 7046−7063

Read Online

ACCESS | Metrics & More | Article Recommendations | Supporting Information

ABSTRACT: **Type 2 alveolar epithelial cell (AEC2) senescence is crucial to the pathogenesis of pulmonary fibrosis (PF). The nicotinamide adenine dinucleotide (NAD^+)-consuming enzyme cluster of differentiation 38 (CD38) is a marker of senescent cells and is highly expressed in AEC2s of patients with PF, thus rendering it a potential treatment target. Umbilical cord mesenchymal stem cell (MSC)-derived extracellular vesicles (MSC-EVs) have emerged as a cell-free treatment with clinical application prospects in antiaging and antifibrosis treatments. Herein, we constructed CD38 antigen receptor membrane-modified MSC-EVs (CD38-ARM-MSC-EVs) by transfecting MSCs with a lentivirus loaded with a CD38 antigen receptor−CD8 transmembrane fragment fusion plasmid to target AEC2s and alleviate PF. Compared with MSC-EVs, the CD38-ARM-MSC-EVs engineered in this study showed a higher expression of the CD38 antigen receptor and antifibrotic miRNAs and targeted senescent AEC2s cells highly expressing CD38 in vitro and in naturally aged mouse models after intraperitoneal administration. CD38-ARM-MSC-EVs effectively restored the NAD^+ levels, reversed the epithelial−mesenchymal transition phenotype, and rejuvenated senescent A549 cells in vitro, thereby mitigating multiple age-associated phenotypes and alleviating PF in aged mice. Thus, this study provides a technology to engineer MSC-EVs and support our CD38-ARM-MSC-EVs to be developed as promising agents with high clinical potential against PF.**

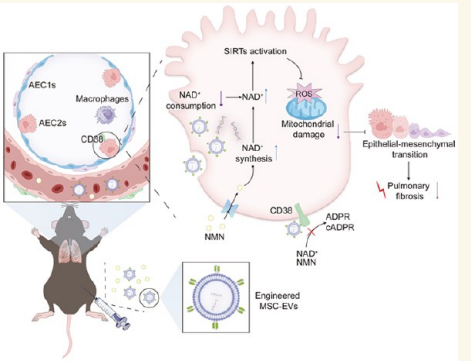

KEYWORDS: *mesenchymal stem cells, extracellular vesicles, CD38, senescence, alveolar epithelial cells, pulmonary fibrosis*

INTRODUCTION

Pulmonary fibrosis (PF) is a chronic, progressive, and aggressive interstitial lung disease characterized by irreversible alveolar structure destruction and interstitial scarring that can impair lung function and lead to death.[1] Although antifibrotic drugs such as pirfenidone[2] and nintedanib[3] can target fibroblasts and inhibit collagen synthesis, they cannot reverse existing fibrosis, promote lung repair, or reduce mortality. Therefore, efficient therapeutic treatments are urgently required.

Cluster of differentiation 38 (CD38) is a transmembrane glycoprotein with multifunctional properties that can facilitate the conversion of nicotinamide adenine dinucleotide (NAD^+) to various metabolites.[4−6] NAD^+ is involved in numerous cellular and molecular processes, and a decline in its availability is a key driving force of aging and age-related degeneration and diseases.[7,8] Thus, restoring NAD^+ levels can delay or even reverse aging and age-related diseases.[9−11] CD38 expression and activity increase with age in various cells, especially in type 2 alveolar epithelial cells (AEC2s) of older people and patients with PF. In addition, CD38 expression has been clinically associated with AEC2 senescence and PF.[12] The repeated injury of the alveolar epithelium decreases epithelial integrity in PF. The alveoli are lined by squamous type 1 AECs

Received: October 26, 2023
Revised: February 9, 2024
Accepted: February 13, 2024
Published: February 21, 2024

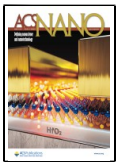

Scheme 1. Schematic Illustration of CD38 Antigen Receptor Membrane-Modified MSC-EVs for Pulmonary Fibrosis[a]

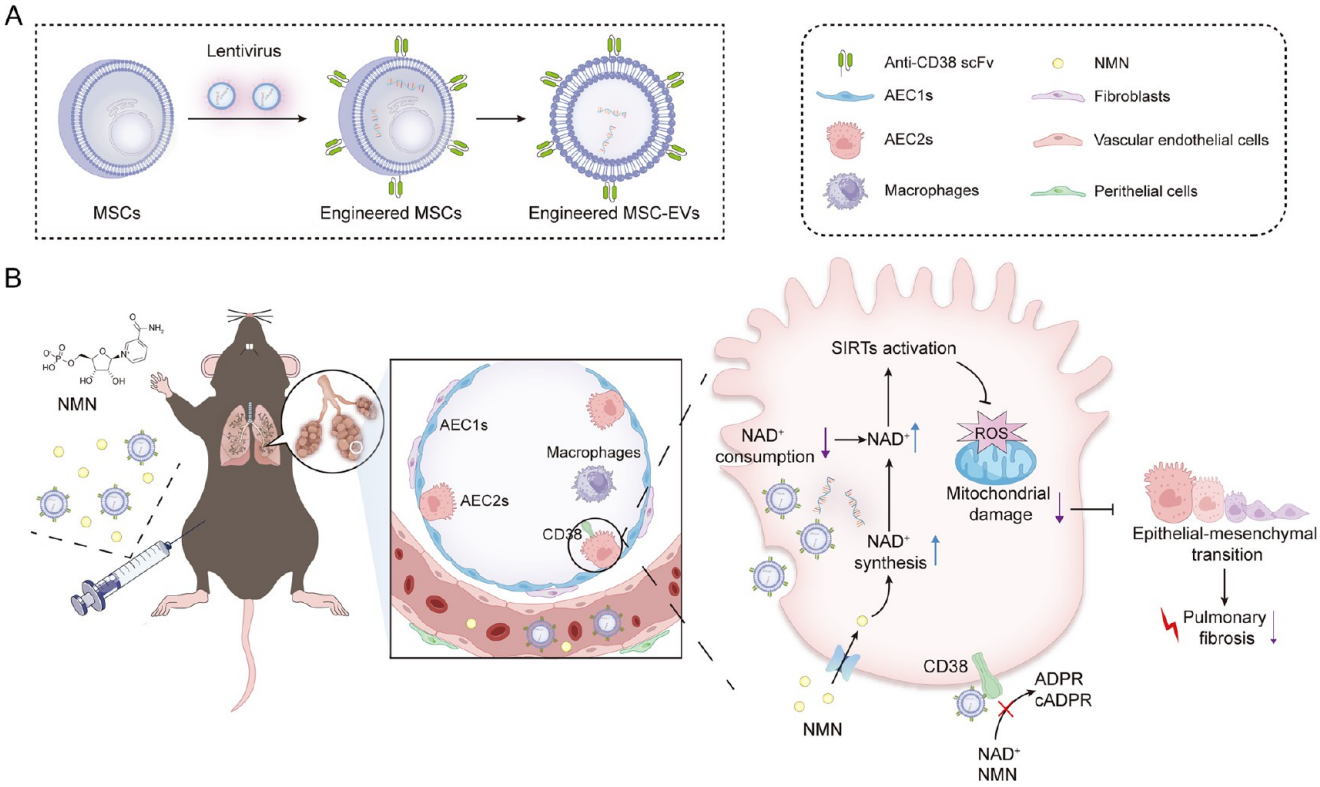

[a](A) Construction of CD38-ARM-MSC-EVs by transfection of lentivirus packaged anti-CD38 scFv plasmid. (B) After intraperitoneal injection, CD38-ARM-MSC-EVs exhibited significant CD38-expression tissue tropism; then, CD38-ARM-MSC-EVs bound to CD38 on the AEC2 surface and blocked CD38-hydrolyzed NAD^+ and NMN. Thus, decreasing NAD^+ consumption and increasing NAD^+ synthesis contributed to the activation of the SIRT family and restored mitochondrial function, which reversed epithelial-mesenchymal transition and alleviated pulmonary fibrosis.

(AEC1s), which allow passive gas diffusion, and cuboidal AEC2s, which support lung function by secreting surfactant proteins.[13] AEC2s are currently viewed as the most critical cell type in PF,[14,15] as senescent AEC2s undergo epithelial−mesenchymal transition (EMT) to transform to fibroblasts and myofibroblasts, inducing excessive extracellular matrix secretion, leading to collagen deposition and lung structure destruction.[14,16,17] CD38 expression promotes AEC2 senescence by reducing intracellular NAD^+ levels and impairing NAD-dependent cellular and molecular activities, thereby mediating PF. Gene knockout or the pharmacological inhibition of CD38 can improve AEC2 senescence and reduce the severity of PF in mice.[12] Therefore, targeting senescent AEC2s with high expression of CD38 antigen ($CD38^{high}$) may be a potential therapeutic strategy for PF. In addition, supplementation with NAD^+ precursors such as nicotinamide mononucleotide (NMN), has been shown to ameliorate aging and fibrosis in various tissues,[18−21] and increasing NAD^+ synthesis and inhibiting NAD^+ consumption has emerged as an important antiaging concept.

Extracellular vesicles (EVs) are membrane-bound vesicles that are released by cells and play a key role in intercellular communication by modulating various signaling pathways through paracrine or endocrine effects.[22,23] EVs derived from mesenchymal stem cells (MSCs) or other sources, such as epithelial cells, endothelial cells, and macrophages, exert anti-PF effects.[24−27] However, poor targeting and low therapeutic efficiency are challenges in using EVs for treating diseases. Recently, engineering to target EVs has attracted widespread attention and is expected to be a promising approach for EV-based treatment. Modifying the membrane surface of EVs,[28,29] surface engineering using single-chain variable fragments (scFv) could be a potential target-specific method. Specific antigen receptor scFv modification can effectively target cells with the same antigen,[30−33] where the chimeric antigen receptor (CAR) technology uses scFv to target tumor cells[34] or senescent cells,[35,36] and CAR-T-cell-derived EVs (CAR-EVs) can selectively target cells.[37−41]

Previous studies have confirmed that umbilical cord MSC-derived EVs (MSC-EVs) can prevent PF.[27] Herein, we used CAR technology to construct CD38 antigen receptor membrane-modified umbilical cord MSC-EVs (CD38-ARM-MSC-EVs) for targeting senescent AEC2s to achieve an antifibrosis effect that can help alleviate PF. Additionally, we investigated whether the engineered CD38-ARM-MSC-EVs could synergistically enhance the anti-PF effects of NMN (Scheme 1).

RESULTS

Construction and Characterization of CD38-ARM-MSC-EVs. First, we engineered MSCs by modifying the CD38 antigen receptor membrane and then isolated EVs expressing the CD38 antigen receptor from these MSCs to target CD38-positive AECs (Figure 1A). Plasmids for the CD8 transmembrane region, CD38 antigen receptor, and CD38 antigen receptor−CD8 transmembrane region were con-

https://doi.org/10.1021/acsnano.3c10547
ACS Nano 2024, 18, 7046−7063

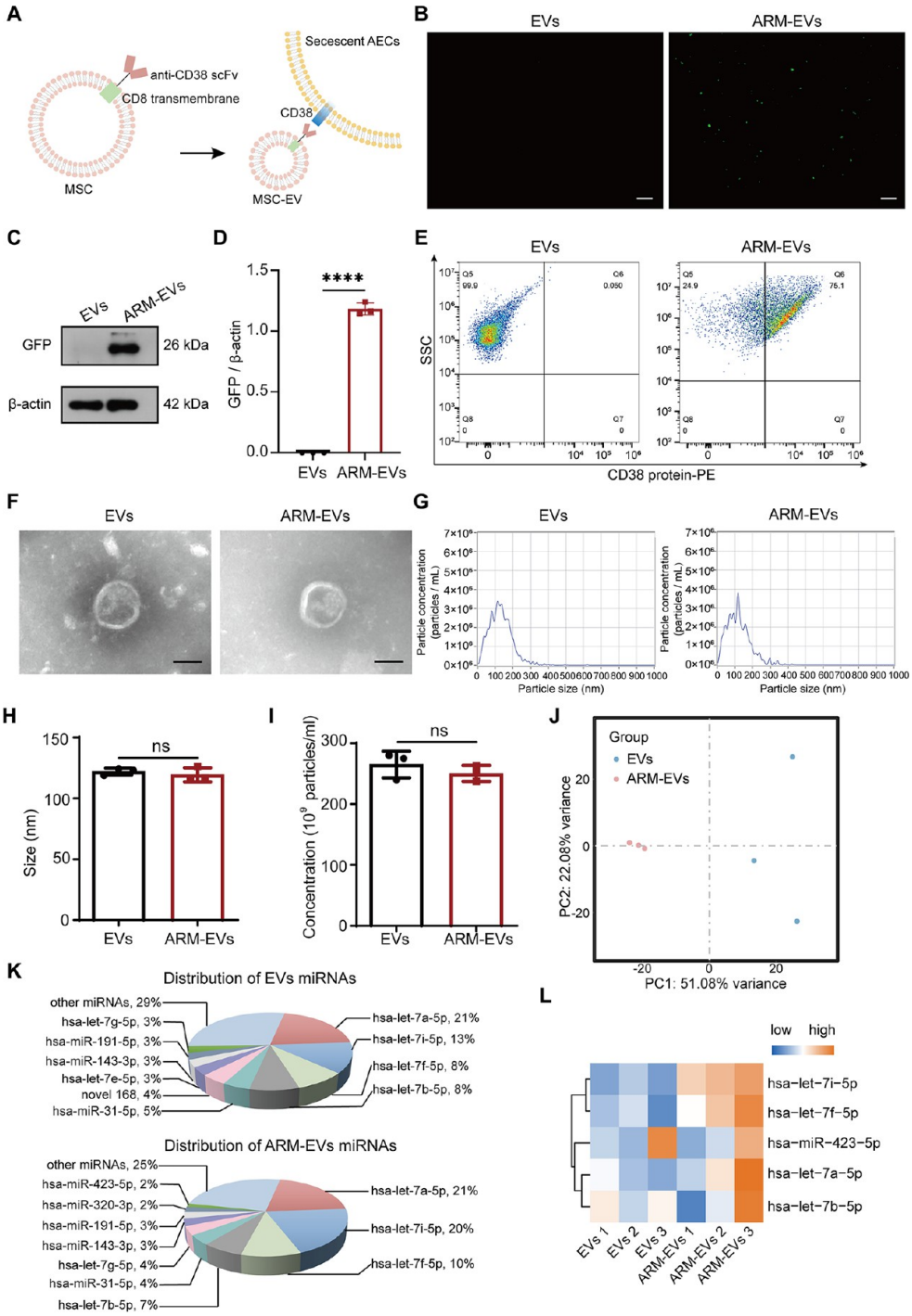

Figure 1. Construction and characterization of CD38-ARM-MSC-EVs. (A) The structure of engineered MSCs and their secreted EVs, including the antigen binding region (scFv) and transmembrane region. Engineered EVs (CD38-ARM-MSC-EVs) can recognize senescence-specific antigens on the surface of senescent cells. (B) Representative fluorescence images showing GFP expression in MSC-EVs and CD38-ARM-MSC-EVs. Scale bars = 50 μm. (C, D) Immunoblots showing GFP expression in EVs. (E) Representative dot plots and overall percentage of CD38-ARM-positive EVs in CD38-ARM-MSC-EVs. (F) Transmission electron microscopy (TEM) micrographs of MSC-EVs and CD38-ARM-MSC-EVs. Scale bars = 50 nm. (G) Size distributions of the MSC-EVs and CD38-ARM-MSC-EVs were determined via nanoparticle tracking analysis (NTA). (H, I) Mean diameter (panel (H)) and concentration (panel (I)) of MSC-EVs and CD38-ARM-MSC-EVs (n = 3) determined via NTA. (J) Principal component analysis (PCA) chart of MSC-EVs and CD38-ARM-MSC-EVs miRNA content. (K) Distribution of the top 10 miRNAs in MSC-EVs (top) and CD38-ARM-MSC-EVs (bottom). (L) Heatmap of miRNAs associated with PF in the top 10 genes of MSC-EV and CD38-ARM-MSC-EV abundance. Data are presented as the means ± SDs. [Legend: (****) $P < 0.0001$; ns, nonsignificant.] In panels (D), (H), and (I), the data were analyzed by using a Student's t-test. [Abbreviations: EVs, MSC-EVs; ARM-EVs, CD38-ARM-MSC-EVs.]

structed and packaged into the lentivirus, following which the lentivirus was transfected into MSCs. Fluorescence and flow cytometry were used to detect whether the MSC membrane carried the CD38 antigen receptor and specifically bound the

https://doi.org/10.1021/acsnano.3c10547
ACS Nano 2024, 18, 7046−7063

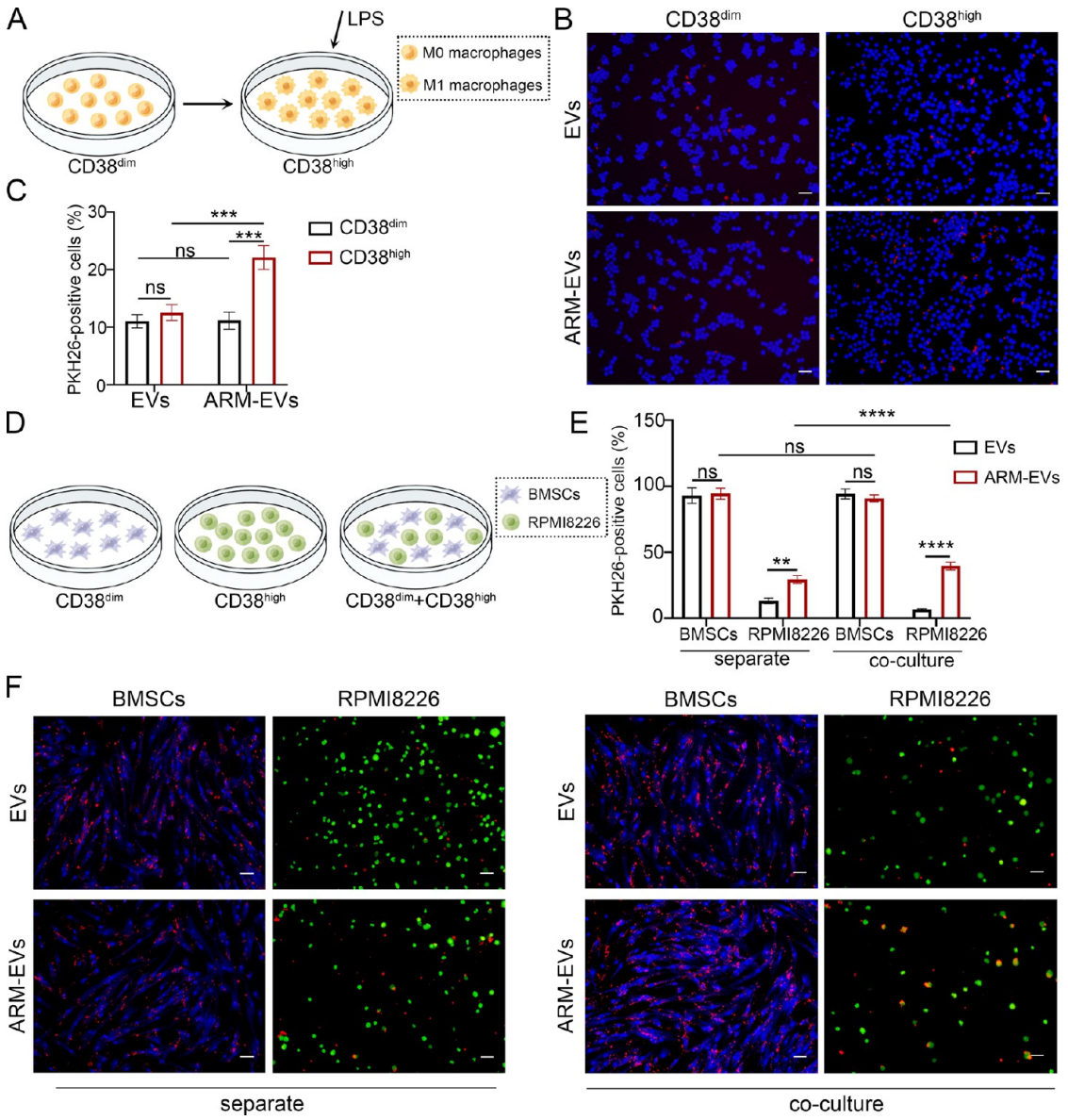

Figure 2. CD38-ARM-MSC-EVs target CD38^{high} cells. (A) RAW264.7 cells (a macrophage cell line, M0) were considered CD38^{dim} cells, and LPS-stimulated RAW264.7 cells (M1) were considered CD38^{high} cells. (B) Representative images showing the cellular internalization of PKH26-stained MSC-EVs and CD38-ARM-MSC-EVs by CD38^{dim} cells (RAW264.7 cells, M0) and CD38^{high} cells (LPS-stimulated RAW264.7 cells, M1). Scale bars = 100 μm. (C) Bar graph showing the PKH26-positive cell ratio (%) in panel (B) (n = 3). (D) BMSC (CD38^{dim} cells, DAPI-labeled, blue) and RPMI8226 cell (CD38^{high} cells, CFSE-labeled, green) culture separately or co-culture. (E) Bar graph showing the targeted cell ratio (%) in panel (F) (n = 3). (F) Representative images show the cellular internalization of PKH26-stained MSC-EVs and CD38-ARM-MSC-EVs by CD38^{dim} cells and CD38^{high} cells after 12 h of incubation. Scale bars = 50 μm for BMSCs, 25 μm for RPMI8226 cells. Data are presented as the means ± SDs. [Legend: (**) P < 0.01, (***) P < 0.001, (****) P < 0.0001, ns, nonsignificant.] Panels (B) and (E) were analyzed by using two-way ANOVA and Bonferroni's multiple comparisons test. [Abbreviations: LPS, lipopolysaccharide; EVs, MSC-EVs; ARM-EVs, CD38-ARM-MSC-EVs; BMSCs, bone marrow MSCs.]

CD38 antigen. Only the cells transfected with the CD38 antigen receptor−CD8 transmembrane region fusion fragment highly expressed the target antigen receptor (Figures S1A and S1B). These engineered MSCs (CD38-ARM-MSCs) exhibited a morphology similar to that of nonengineered MSCs (Figure S2A) and expressed CD29, CD44, CD90, CD73, and CD105 but lacked the expression of CD34, CD45, and CD31 (Figure S2B), with the capacity to differentiate into osteogenic and adipogenic lineages (Figures S2C and S2D).

Next, EVs derived from the CD38-ARM-MSCs (CD38-ARM-MSC-EVs) were characterized. EVs were isolated from the supernatants of the engineered and nonengineered MSCs via ultracentrifugation. GFP expression in CD38-ARM-MSC-EVs was confirmed via laser confocal microscopy (Figure 1B) and Western blotting (Figures 1C and 1D). Compared with MSC-EVs, CD38-ARM-MSC-EVs effectively expressed anti-CD38-scFv on their surface (Figure 1E), indicating the successful construction of CD38-ARM-MSC-EVs highly expressing surface anti-CD38-scFv and sharing a similar morphology, size, common EV markers (CD9, CD63, CD81, and TSG101), and MSC surface markers (CD73, CD90, and CD105) with unmodified MSC-EVs (see Figure 1F−I, as well as Figures S2E and S2F).

https://doi.org/10.1021/acsnano.3c10547
ACS Nano 2024, 18, 7046−7063

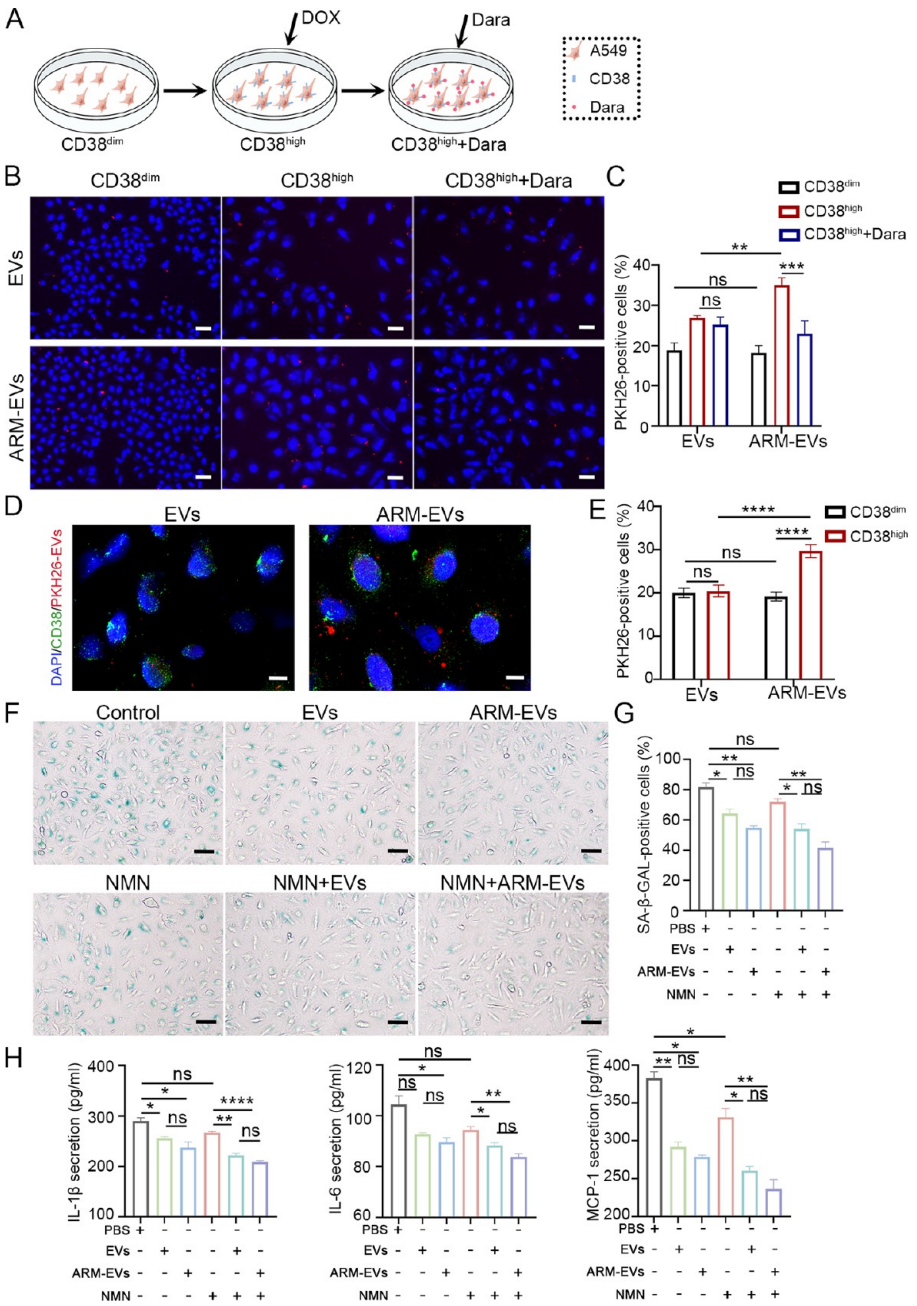

Figure 3. CD38-ARM-MSC-EVs target and rejuvenate senescent A549 cells. (A) Nonsenescent A549 cells were considered CD38^{dim} cells, and senescent A549 cells induced by 0.25 μM DOX were considered CD38^{high} cells. In addition, senescent A549 cells induced by 0.25 μM DOX pretreatment with daratumumab to block surface CD38 were considered CD38^{high} + Dara cells. (B) Representative images showing the cellular internalization of PKH26-stained MSC-EVs and CD38-ARM-MSC-EVs by CD38^{dim} cells (nonsenescent A549 cells), CD38^{high} cells (0.25 μM DOX-induced senescent A549 cells), and CD38^{high} cells (senescent A549 cells induced by 0.25 μM DOX) pretreated with daratumumab. Scale bars = 100 μm. (C) Bar graph showing the targeted cell ratio (%) in panel (B) (n = 3). (D) Representative images showing the cellular internalization of PKH26-stained MSC-EVs and CD38-ARM-MSC-EVs by CD38-positive cells and CD38-negative cells among senescent A549 cells induced by 0.25 μM DOX. Scale bars = 50 μm. (E) Bar graph showing the targeted cell ratio (%) in panel (D) (n = 3). (F, G) Representative micrographs of SA-β-GAL staining (F) and quantitative analysis (G) of SA-β-gal-positive senescent A549 cells (n = 3). Scale bar = 100 μm. (H) Detection of the secreted levels of IL-1β, IL-6, and MCP-1 in senescent A549 cells by ELISA. Data are presented as the means ± SDs. [Legend: (*) P < 0.05, (**) P < 0.01, (***) P < 0.001, (****) P < 0.0001, ns, nonsignificant.] Panels (C) and (E) were analyzed by using two-way ANOVA and Bonferroni's multiple comparisons test. Panels (G) and (H) were analyzed by using one-way ANOVA and Bonferroni's multiple comparisons test. [Abbreviations: DOX, doxorubicin; Dara, daratumumab; EVs, MSC-EVs; ARM-EVs, CD38-ARM-MSC-EVs.]

Due to the key roles of miRNA in EVs, we further performed global small RNA deep-sequencing of CD38-ARM-MSC-EVs and MSC-EVs, focusing on and comparing the 10 most abundant miRNAs (Figures 1J and 1K). Our study revealed that 5 of the 10 miRNAs, including the let-7 family and miR-423-5p, were involved in anti-PF (Figure 1L).[25,42−44] Among them, let-7i-5p and let-7f-5p were significantly upregulated in CD38-ARM-MSC-EVs but were downregulated

https://doi.org/10.1021/acsnano.3c10547
ACS Nano 2024, 18, 7046−7063

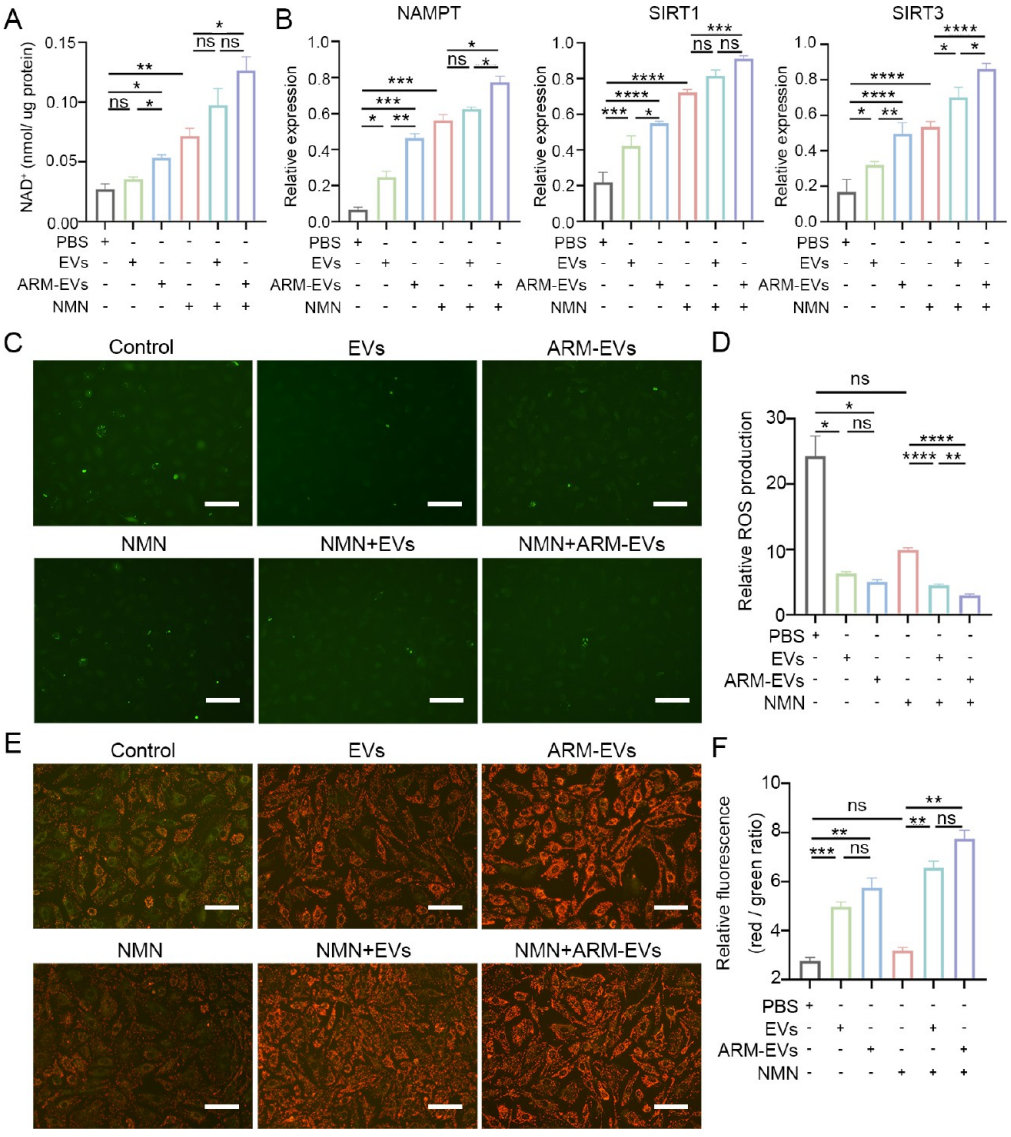

Figure 4. CD38-ARM-MSC-EVs restore NAD^+ levels and reverse EMT in senescent A549 cells. Senescent A549 cells were induced with 0.25 μM DOX. These senescent cells were treated with PBS, MSC-EVs (EVs), CD38-ARM-MSC-EVs (ARM-EVs), NMN, MSC-EVs with NMN (NMN + EVs), or CD38-ARM-MSC-EVs with NMN (NMN + ARM-EVs). (A) Detection of the intracellular NAD^+ concentration in senescent A549 cells. (B) qPCR analysis of the expression levels of *NAMPT*, *SIRT1*, and *SIRT3* in senescent A549 cells. (C) Detection of ROS levels in senescent A549 cells. Scale bars = 50 μm. (D) Bar graph showing the relative ROS production in panel (C) (n = 3). (E) Detection of the mitochondrial membrane potential in senescent A549 cells. Scale bars = 50 μm. (F) Bar graph showing the mitochondrial membrane potential in panel (E) (n = 3). Data are presented as the means ± SDs. [Legend: (*) $P < 0.05$, (**) $P < 0.01$, (***) $P < 0.001$, (****) $P < 0.0001$, ns, nonsignificant.] Panels (A)−(F) were analyzed by using one-way ANOVA and Bonferroni's multiple comparisons test. [Abbreviations: EVs, MSC-EVs; ARM-EVs, CD38-ARM-MSC-EVs.]

in PF lung samples, according to the miRNA microarray analysis (GSE32358 dataset). These findings demonstrate the successful construction of CD38-ARM-MSC-EVs with potential antifibrotic effects.

CD38-ARM-MSC-EVs Target $CD38^{high}$ Cells. To test whether CD38-ARM-MSC-EVs selectively targeted $CD38^{high}$ cells, RAW264.7 cells (a macrophage cell line, M0)[45] and human bone marrow MSCs (BMSCs)[46] were cultured as $CD38^{dim}$ cells (Figures S3A−S3D) and lipopolysaccharide (LPS)-stimulated RAW264.7 cells (M1)[45] and RPMI8226 cells (a myeloma cell line)[47] were cultured as $CD38^{high}$ cells (Figures S3A−S3D) with unmodified MSC-EVs and CD38-ARM-MSC-EVs. The uptake of PKH26-labeled CD38-ARM-MSC-EVs by DAPI-labeled M1 cells was significantly greater than that of PKH26-labeled unmodified MSC-EVs, whereas no difference was observed between the uptake of the two types of EVs by M0 cells (Figure 2A−C). Similarly, CFSE-labeled RPMI8226 cells took up significantly more PKH26-labeled CD38-ARM-MSC-EVs than did PKH26-labeled unmodified MSC-EVs, while no apparent difference in uptake was observed in DAPI-labeled BMSCs (Figure 2D−F). To investigate CD38-ARM-MSC-EVs targeting $CD38^{high}$ cells, BMSCs and CFSE-labeled RPMI8226 cells were co-cultured, followed by incubation with PKH26-labeled CD38-ARM-MSC-EVs or unmodified MSC-EVs for 12 h. Accordingly, the uptake of CD38-ARM-MSC-EVs by RMPMI8226 cells remained significantly greater than that by unmodified MSC-EVs, whereas no difference in BMSC uptake was observed

https://doi.org/10.1021/acsnano.3c10547
ACS Nano 2024, 18, 7046−7063

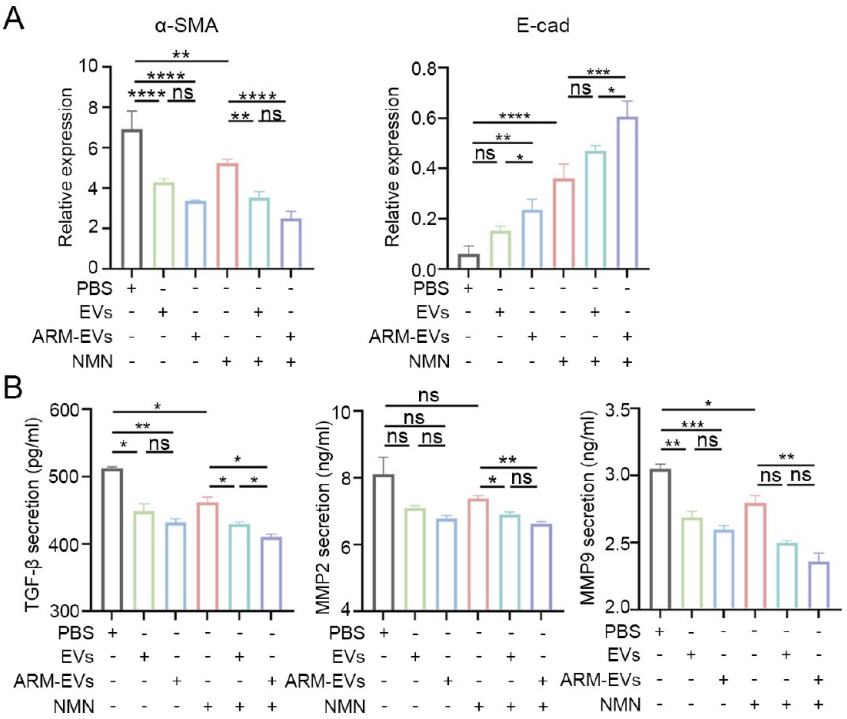

Figure 5. CD38-ARM-MSC-EVs reverse EMT in senescent A549 cells. Senescent A549 cells were induced with 0.25 μM DOX. These senescent cells were treated with PBS, MSC-EVs (EVs), CD38-ARM-MSC-EVs (ARM-EVs), NMN, MSC-EVs with NMN (NMN + EVs), or CD38-ARM-MSC-EVs with NMN (NMN + ARM-EVs). (A) qPCR analysis of the expression levels of *α-SMA* and *E-cad* in senescent A549 cells. (B) Detection of the secreted levels of TGF-β, MMP2, and MMP9 in A549 cells by ELISA. Data are presented as the means ± SDs. [Legend: (*) $P < 0.05$, (**) $P < 0.01$, (***) $P < 0.001$, (****) $P < 0.0001$, ns, nonsignificant.] Panels (A) and (B) were analyzed by using one-way ANOVA and Bonferroni's multiple comparisons test. [Abbreviations: EVs, MSC-EVs; ARM-EVs, CD38-ARM-MSC-EVs.]

between the two types of EVs, although the basic uptake of these EVs by BMSCs was obviously higher than that by RPMI8226 cells (Figure 2D−F). These data demonstrate that CD38-ARM-MSC-EVs could target CD38^{high} cells.

CD38-ARM-MSC-EVs Target and Rejuvenate Senescent AEC2 A549 Cells. Senescence of AEC2s with increased CD38 expression is the key pathological hallmark of lung fibrosis.[12,14] Therefore, we selected A549 cells, an AEC2 cell line, to test whether CD38-ARM-MSC-EVs could target senescent AECs. As previously reported,[48] different concentrations of doxorubicin (DOX) were used to induce A549 cell senescence as an in vitro cell model of AEC senescence; senescence-associated β-galactosidase (SA-β-GAL) and senescence-associated secretory phenotype (SASP) as senescence markers were consequently detected via staining and enzyme-linked immunosorbent assay (ELISA), respectively. The surface expression of CD38 in DOX-induced senescent AEC2 A549 cells was assayed by using qPCR, Western blotting, flow cytometry, and immunofluorescence. DOX treatment successfully induced cell senescence and increased CD38 expression in A549 cells in a dose-dependent manner (Figures S4A−S4I and S5A−S5F). Since there was similar CD38 expression but better cell viability, A549 cells treated with 0.25 μM instead of 0.5 μM DOX were used as an in vitro senescent AEC2 model (Figures S4A−S4C and S5B−S5F).

Noninduced A549 cells (CD38^{dim} cells) and 0.25 μM DOX-induced A549 cells (CD38^{high} cells) were subsequently used to determine the capacity of CD38-ARM-MSC-EVs to target senescent AECs (Figure 3A). Similar to CD38^{high} M1 and RPMI8226 cells, CD38^{high} A549 cells also took up significantly more PKH26-labeled CD38-ARM-MSC-EVs than CD38^{dim} A549 cells, with no difference between them when cultured with unmodified MSC-EVs (Figures 3B and 3C). To investigate whether CD38-ARM-MSC-EVs bind to the surface CD38 antigen on CD38^{high} A549 cells, the cells were pretreated with daratumumab (a CD38 monoclonal antibody) to block cell surface CD38 and then incubated with CD38-ARM-MSC-EVs or MSC-EVs. Notably, after daratumumab blocking, the proportion of PKH26-positive CD38^{high} cells after incubation with CD38-ARM-MSC-EVs was significantly diminished (35.03% vs 22.93%, $p = 0.0001$), while no change in the uptake efficiency of unmodified MSC-EVs was observed (26.85% vs 25.19%, $p = 0.9976$; see Figures 3B and 3C). CD38 immunofluorescence staining revealed that CD38^{high} cells took up more CD38-ARM-MSC-EVs than CD38^{dim} cells, with no difference in the uptake of MSC-EVs (see Figures 3D and 3E). These findings support the notion that DOX-induced senescent A549 cells highly express surface CD38 antigen and that CD38-ARM-MSC-EVs can target these CD38^{high} cells in vitro.

Next, we explored whether CD38-ARM-MSC-EV treatment could rejuvenate senescent CD38^{high} A549 cells and synergistically enhance the antiaging effect of NMN on these senescent cells. DOX-induced senescent A549 cells were treated continuously for 2 days with CD38-ARM-MSC-EVs (ARM-EVs), unmodified MSC-EVs (EVs), NMN and CD38-ARM-MSC-EVs (NMN + ARM-EVs), NMN and unmodified MSC-EVs (NMN + EVs), and phosphate-buffered saline (PBS; control). SA-β-Gal staining and ELISA detection of SASPs, such as IL-1β, IL-6, and MCP-1, showed that CD38-ARM-MSC-EVs significantly decreased the levels of SAPSs compared with those in the control, whereas unmodified MSC-EVs did

https://doi.org/10.1021/acsnano.3c10547
ACS Nano 2024, 18, 7046−7063

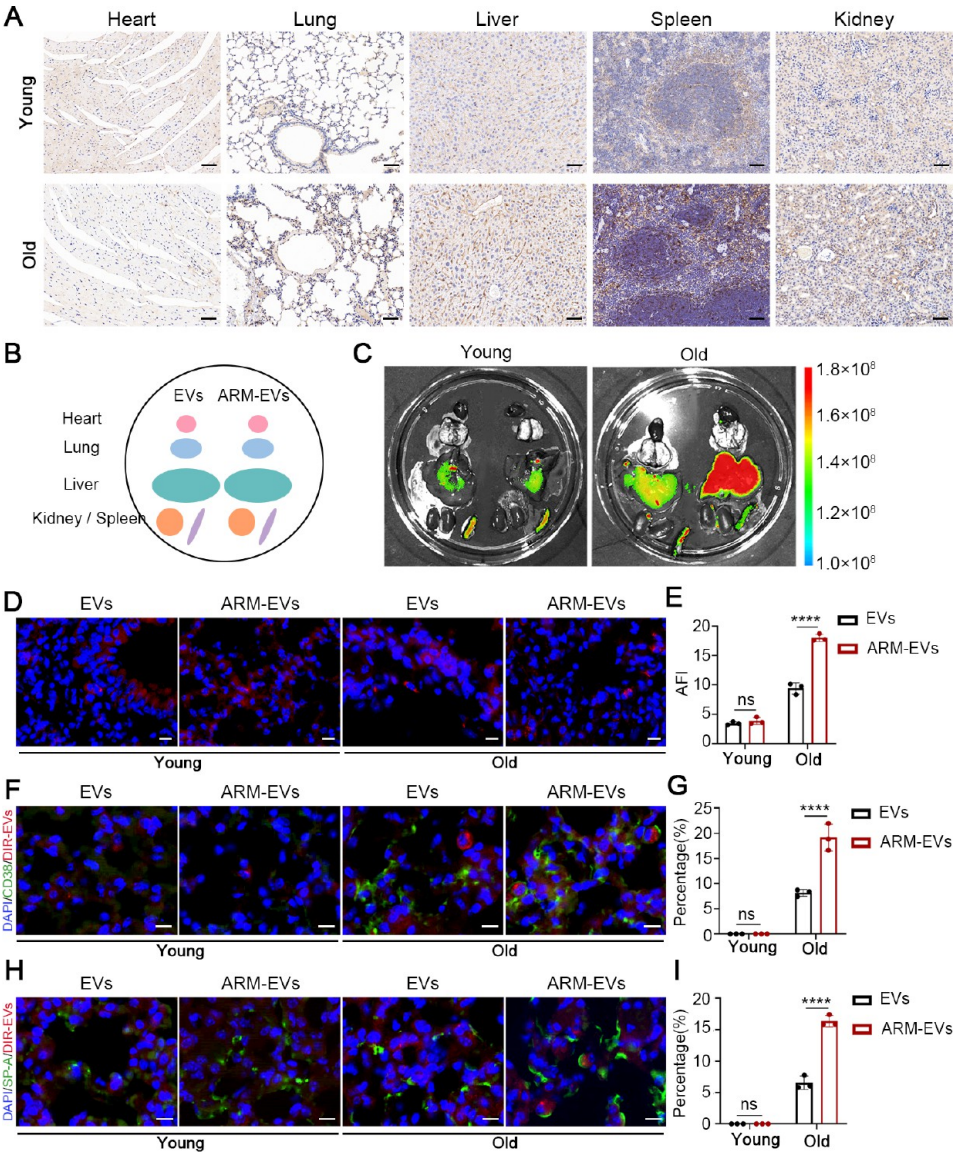

Figure 6. CD38-ARM-MSC-EVs target CD38^{high} cells and AEC2s in naturally old mice. (A) Immunohistochemical staining of CD38 in 3-month-old mice and 18-month-old mice. Scale bars = 50 μm. (B) Schematic diagram of the distribution of each organ. (C) Images of the major organs of young and old mice 24 h after intraperitoneal injection of DiR-labeled EVs. (D) Representative images of the lung sections. Scale bar = 10 μm. (E) Quantification of the average fluorescence intensity in the lung sections in panel (D) (n = 3). (F) Images of stained lung sections from young and old mice 24 h after intraperitoneal injection of DiR-labeled EVs with CD38 (green). Scale bar = 10 μm. (G) The percentages of CD38-positive cells that engulfed DiR-labeled EVs in the lung tissue sections in panel (F) (n = 3). (H) Images of stained lung sections from young and old mice 24 h after intraperitoneal injection of DiR-labeled EVs with SP-A (green). Scale bar = 10 μm. (I) The percentages of AEC2s (SP-A-positive cells) that engulfed DiR-labeled EVs in the lung tissue sections in panel (H) (n = 3). Data are presented as the means ± SDs. [Legend: (****) P < 0.0001, ns, nonsignificant.] Panels (E), (G), and (I) were analyzed by using two-way ANOVA and Bonferroni's multiple comparisons test. [Abbreviations: AFI, average fluorescence intensity; EVs, MSC-EVs; ARM-EVs, CD38-ARM-MSC-EVs; SP-A, surfactant protein A.]

not obviously decrease the IL-6 concentration (Figure 3F−H). Furthermore, the levels of SA-β-Gal, IL-1β, or IL-6 did not significantly decrease in the NMN group compared with those in the control group, while the levels of these senescence-related markers were significantly reduced in the NMN + ARM-EV and NMN + EV combination groups compared to those in the NMN group (see Figure 3F−H). The levels of these senescence-related markers in CD38-ARM-MSC-EVs trended toward improvement compared to those in the unmodified MSC-EVs with or without NMN, although no statistically significant difference was found between these two types of EVs. These data show that CD38-ARM-MSC-EVs can target and rejuvenate CD38^{high} A549 cells and synergistically enhance the antiaging effect of NMN.

CD38-ARM-MSC-EVs Restore NAD$^+$ Levels and Reverse EMT in Senescent A549 Cells. CD38 increases during aging, decreasing NAD$^+$ levels and causing subsequent mitochondrial dysfunction in a sirtuins (SIRT)-dependent manner.[4] CD38 also metabolizes the NAD$^+$ precursor NMN and regulates the response to NAD$^+$ replacement therapies.[5] To confirm the effect of our CD38-ARM-MSC-EVs on NAD$^+$ levels and metabolism in senescent AEC2 A549 cells, the levels of NAD$^+$ and *NAMPT*, *SIRT1*, and *SIRT3* were evaluated, and mitochondrial function was assessed based on the level of

https://doi.org/10.1021/acsnano.3c10547
ACS Nano 2024, 18, 7046−7063

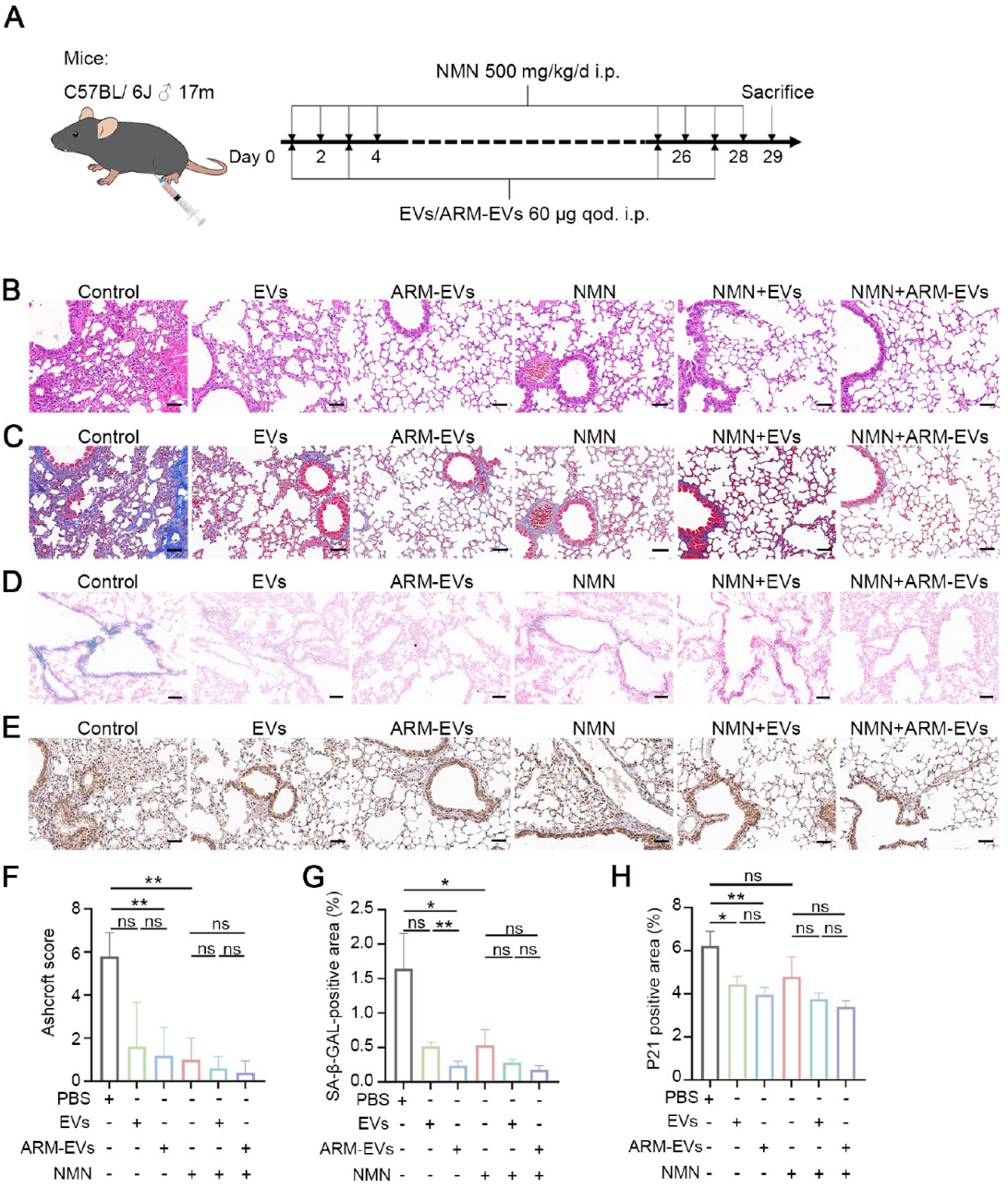

Figure 7. CD38-ARM-MSC-EVs attenuate lung fibrosis in naturally aged mice. (A) Schematic of the protocol for treating old mice with EVs and NMN. (B, C) Hematoxylin and eosin (H&E) (panel (B)) and Masson's trichrome (panel (C)) staining were performed on representative lung tissue sections from each group of treated mice (n = 5). Scale bar = 50 μm. (D) Representative images of stained SA-β-gal-positive areas (n = 5). Scale bar = 100 μm. (E) Immunohistochemical staining of P21 in representative lung sections (n = 5). Scale bar = 50 μm. (F) Quantification of fibrosis by the Ashcroft score (n = 5). (G) Bar graph showing the ratio of SA-β-gal-positive areas (%) in panel (D) (n = 5). (H) Quantification of the P21-positive area (%) in panel (E) (n = 5). Data are presented as the means ± SDs. [Legend: (*) P < 0.05, (**) P < 0.01, ns, nonsignificant.] Panels (F)−(H) were analyzed by using one-way ANOVA and Bonferroni's multiple comparisons test. [Abbreviations: EVs, MSC-EVs; ARM-EVs, CD38-ARM-MSC-EVs.]

reactive oxygen species (ROS) and mitochondrial membrane potential.

We found that CD38-ARM−MSC−EVs could regulate NAD^+ metabolism by increasing NAD^+ levels, which promoted *NAMPT*, *SIRT1*, and *SIRT3* expression (Figures 4A, and 4B), and alleviate mitochondrial dysfunction by reducing the ROS content and increasing mitochondrial membrane potential levels (Figure 4C−F). Although the unmodified MSC-EVs also showed these effects, CD38-ARM−MSC−EVs more significantly restored the NAD^+ levels. Furthermore, CD38-ARM-MSC-EVs enhanced the effect of NMN on the levels of NAD^+, *NAMPT*, *SIRT1*, *SIRT3*, and ROS and the mitochondrial membrane potential, while the unmodified MSC-EVs failed to enhance the levels of NAD^+, *NAMPT*, or *SIRT1*. Additionally, CD38-ARM-MSC-EVs exhibited more significant effects on the levels of *NAMPT*, *SIRT3*, and ROS than the unmodified MSC-EVs, when combined with NMN. These results indicate that CD38-ARM-MSC-EVs reversed the NAD^+ decline more than the unmodified MSC-EVs and had potential advantages in NAD^+ regulation with or without NMN (Figure 4A−F).

https://doi.org/10.1021/acsnano.3c10547
ACS Nano 2024, 18, 7046−7063

EMT is a major feature of PF wherein senescence regulates the secretion of PF-related cytokines, such as transforming growth factor (TGF)-β, and α-smooth muscle actin (α-*SMA*), E-cadherin (*E-cad*), MMP2, and MMP9, by AECs to promote EMT, leading to collagen deposition and fibrosis formation. We found that CD38-ARM-MSC-EVs inhibited EMT in senescent A549 cells, compared with that in the PBS control, as manifested by the downregulation of α-*SMA*, upregulation of that of *E-cad*, and inhibition of the secretion of profibrotic factors such as TGF-β and MMP9, whereas the unmodified MSC-EVs failed to downregulate the expression of *E-cad* (Figures 5A and 5B). NMN also inhibited EMT and reduced the secretion of profibrotic cytokines, while CD38-ARM-MSC-EVs synergistically enhanced the effects of NMN on the expression levels of α-*SMA*, *E-cad*, TGF-β, MMP2, and MMP9, whereas the unmodified MSC-EVs failed in the effects on *E-cad* and MMP9 (Figures 5A and 5B). Additionally, CD38-ARM-MSC-EVs exhibited stronger effects on the levels of *E-cad* and TGF-β than did the unmodified MSC−EVs when combined with NMN.

These findings indicate that CD38-ARM-MSC-EVs could restore NAD^+ levels, reverse mitochondrial function, and regulate EMT in senescent A549 cells with greater potential than the unmodified MSC-EVs for antiaging and antifibrotic effects on PF in vitro.

CD38-ARM-MSC-EVs Target AEC2 in Naturally Aged Mice. Next, we investigated whether CD38-ARM-MSC-EVs could target $CD38^{high}$ cells in vivo. Similar to the findings of previous reports,[5,12,49] we detected elevated CD38 expression via immunohistochemical and immunofluorescence staining in the lung, liver, and spleen tissues of aged mice (17 months old) compared with that in young mice (3 months old) while the heart and kidney tissues did not exhibit these changes (see Figure 6A, as well as Figure S7A). We then observed the biodistribution of the two types of EVs in aged mice. Two hours after 100 μg of DiR-labeled EVs was intraperitoneally administered to 18-month-old mice, both types of EVs primarily accumulated in the spleen but not in the lung, with a higher retention of CD38-ARM-MSC-EVs (Figures S7B and S7C) being observed at the entire organ level. We further intraperitoneally administered 100 μg PKH26-labeled EVs to mice and observed their distribution in organ tissue sections. Both types of EVs preferentially accumulated in the lung, liver, and spleen tissues, compared with that in the heart and kidney tissues, while more CD38-ARM-MSC-EVs than MSC-EVs were found in the $CD38^{high}$ tissues, such as the lung, liver, and spleen tissues (Figures S7D and S7E). Furthermore, CD38-ARM-MSC-EVs were mainly bound to CD38-positive cells in the lung tissues, especially AEC2s marked by surfactant protein A (SP-A), while MSC-EVs exhibited a weaker binding ability (Figure S7F−S7I).

To better understand the biodistribution of EVs in aged mice, DiR-labeled CD38-ARM-MSC-EVs and unmodified MSC-EVs were intraperitoneally administered to young and old mice, respectively. To ensure that an adequate amount of EVs was provided to the tissues, we increased the dose of EVs to 150 μg and extended the detection time to 24 h and observed that both types of EVs primarily accumulated in the spleen and liver rather than in the lung in both types of mice (see Figures 6B and 6C). In the old mice, compared to the unmodified MSC-EVs, a higher retention of CD38-ARM-MSC-EVs in the liver was observed, and tissue section analysis revealed that CD38-ARM-MSC-EVs were more significantly enriched in $CD38^{high}$ tissues (the liver, spleen, lung, and kidney; see Figures 6D and 6E, as well as Figures S8A and S8B). Accordingly, more CD38-ARM-MSC-EVs were found in CD38-positive cells and SP-A-positive AEC2s in the lung tissue sections than unmodified MSC-EVs (see Figure 6F−I). Interestingly, these differences could not be found in the young mice. We found that the number of both types of EVs was significantly lower in young mice than in old mice, which could be attributed to different age-related pharmacokinetics.

Thus, compared to MSC-EVs, CD38-ARM-MSC-EVs preferentially accumulated in CD38-positive tissues and targeted AEC2s in aged mice.

CD38-ARM-MSC-EVs Mitigate Multiple Age-Associated Mouse Phenotypes. As CD38 demonstrated a targeting role in antiaging treatment, we subsequently confirmed whether CD38-ARM-MSC-EVs could mitigate age-associated mouse phenotypes and show a significant synergistic effect with NMN, a drug with antiaging effects.[20,21] Hence, 17-month-old C57BL/6J mice were divided into five treatment groups: MSC-EVs, CD38-ARM-MSC-EVs, NMN, MSC-EVs with NMN, and CD38-ARM-MSC-EVs with NMN, with PBS as the control (Figure 7A).

Body weight measurements indicated a mild difference among all of the groups (Figure S9A). Compared with that in the control, a significant decline in the secretion of SASP factors, such as IL-1β, IL-6, and TNF-α, was detected in mice of the CD38-ARM-MSC-EV group, whereas no significant changes were detected in IL-6 secretion in the MSC-EV group (Figure S9B). NMN alone did not significantly reduce IL-1β and IL-6 levels, compared with those in the control; however, the levels of IL-1β, IL-6, and TNF-α were markedly reduced in the NMN + ARM-EV group, compared with those in the NMN group. Conversely, the NMN + MSC-EVs group did not exhibit reduced levels of IL-1β, compared to those in the NMN group. In particular, the CD38-ARM-MSC-EVs with NMN group showed the strongest reduction in the secretion of SASP factors and exhibited a stronger synergistic effect than the MSC-EVs with NMN group (Figure S9B). Treatment-induced changes similar to those induced by SASP factors were observed for the plasma levels of liver functional markers, including alanine aminotransferase (ALT) and glutamic oxaloacetic transaminase (AST), and kidney functional markers, including creatinine (CRE) and uric acid (UA). When combined with NMN, numerical differences in AST and CRE levels and significant differences in ALT and UA levels were observed between the two combined groups (see Figures S9C and S9D). These data support the capacity of CD38-ARM-MSC-EVs to potentially mitigate age-associated phenotypes in aged mice, especially when combined with NMN.

CD38-ARM-MSC-EVs Alleviate Lung Fibrosis in Naturally Aged Mice. We then evaluated age-associated histological changes in mouse organs using hematoxylin and eosin (H&E) staining. Typical age-associated changes were found in both CD38-negative tissues (the heart) and CD38-positive tissues (the liver, spleen, and kidney), with no apparent difference between the treated groups and the control (see Figures S10A−S10D). However, Masson staining of kidney tissues did not reveal any apparent reductions in the deposition of fibers in all of the treated groups. SA-β-GAL staining revealed significant decreases in all of the treated groups, with the largest change in the NMN + CD38-ARM-MSC-EV group and no differences between the MSC-EV and CD38-ARM-MSC-EV groups (Figures S10E−S10H).

https://doi.org/10.1021/acsnano.3c10547
ACS Nano 2024, 18, 7046−7063

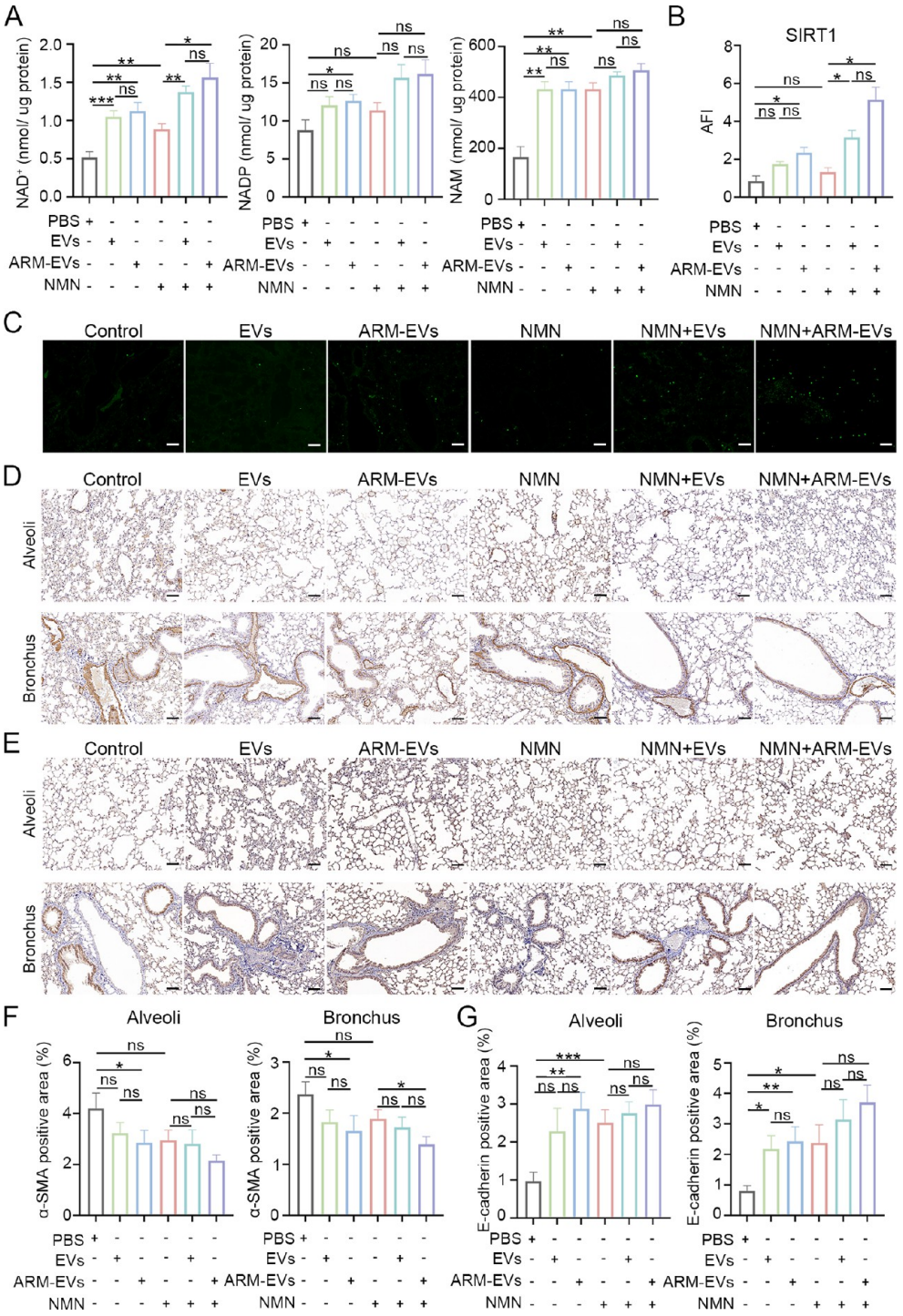

Figure 8. CD38-ARM-MSC-EVs reverse NAD^+ decline and suppress EMT in the lung tissues of old mice. (A) NAD^+, NADP, and NAM levels were measured in lung tissues from each group of treated mice (n = 5). (B) Quantification of the fluorescence intensity of the tissue sections in panel (C) (n = 5). (C) Immunofluorescence staining of SIRT1 in representative lung sections (n = 5). Scale bar = 100 μm. (D, E) Immunohistochemical staining of *α-SMA* (panel (D)) and *E-cad* (panel (E)) in representative lung sections (n = 5). Scale bar = 100 μm. (F, G) Quantification of the *α-SMA*-positive area (panel (F)) and *E-cad*-positive area (panel (G)) (%) in panels (D) and (E) (n = 5). Data are presented as the means ± SDs. [Legend: (*) $P < 0.05$, (**) $P < 0.01$, (***) $P < 0.001$, ns, nonsignificant.] Panels (A)−(G) were analyzed by using one-way ANOVA and Bonferroni's multiple comparisons test. [Abbreviations: EVs, MSC-EVs; ARM-EVs, CD38-ARM-MSC-EVs.]

Since CD38-ARM-MSC-EVs could target and rejuvenate senescent AEC A549 cells in vitro, we focused on changes in the lung tissues. The disordered lung structure of alveolar collapse, pulmonary interstitial thickening, and a high level of inflammatory cell infiltration in aged mice in the control group were obviously alleviated in all of the treatment groups (Figure 7B). Additionally, Masson trichrome staining revealed that aging-related PF was attenuated, and the immunohistochemical staining of SA-β-GAL and P21 revealed notably reduced expression of the two senescence markers (Figure 7C−F) in these groups, compared with that in the control. For further analysis of the effects, a comparable bar graph of the Ashcroft

https://doi.org/10.1021/acsnano.3c10547
ACS Nano 2024, 18, 7046−7063

score[50] was conducted, which showed that the CD38-ARM-MSC-EV group exhibited significantly lower scores, whereas the MSC-EV group exhibited lower scores without statistical significance, compared to the control group. This phenomenon was also found in SA-β-GAL activity changes, where the CD38-ARM-MSC-EV group presented significantly decreased activity, compared with the MSC-EV group. The NMN group exhibited significantly decreased changes in the Ashcroft scores and SA-β-GAL activity compared to the control, and there were numerically but not statistically different decreases between the two combination groups (see Figures 7F and 7G). For P21 expression, the CD38-ARM-MSC-EV and MSC-EV groups had a marked decrease, compared with the control group, without a significant difference between these two EV-treated groups, and no statistically significant reductions were observed in the NMN group (Figure 7H). Thus, CD38-ARM-MSC-EVs could alleviate aging-related PF with more potentially beneficial effects than MSC-EVs.

We further detected the effects of CD38-ARM-MSC-EVs on NAD^+ metabolism and EMT in these lung tissues. We detected the levels of NAD^+, NADP, NAM, and SIRT1 in lung tissue, as well as the expression levels of *α-SMA* and *E-cad*. We found that CD38-ARM-MSC-EVs could efficiently regulate NAD^+ metabolism in the lung tissue, compared with the control, as shown by increased levels of NAD^+, NADP, NAM, and SIRT1, while the unmodified MSC-EVs failed to significantly regulate the levels of NADP and SIRT1. No significant differences were present in the levels of NAD^+, NADP, NAM, or SIRT1 between the two types of EVs, although they significantly enhanced the increasing effect of NMN on the levels of NAD^+ and SIRT1 with no significant differences between the two combination groups (see Figure 8A−C). In addition, compared with the control, CD38-ARM-MSC-EVs down-regulated the expression levels of *α-SMA* and upregulated those of *E-cad* in the alveoli and bronchus tissues; however, MSC-EVs only upregulated *E-cad* expression levels in the bronchus tissues; moreover, there was no difference between the two types of EVs. For *α-SMA* expression in the bronchus tissues, CD38-ARM-MSC-EVs but not MSC-EVs showed a significantly enhanced effect with NMN. When combined with NMN, the effects of these EVs did not obviously differ from those of MSC-EVs on any of the EMT markers (see Figure 8D−G). These results indicate that CD38-ARM-MSC-EVs could potentially increase NAD^+ levels and inhibit EMT in the epithelial barrier of aged lung tissues to prevent the development of fibrosis.

DISCUSSION

In this study, we successfully constructed CD38-ARM-MSC-EVs by transfecting MSCs with lentivirus loaded with a CD38 antigen receptor−CD8 transmembrane fragment fusion plasmid. CD38-ARM-MSC-EVs can target $CD38^{high}$ cells to rejuvenate senescent AEC2s in vitro and attenuate PF in aged mice alongside restoring NAD^+ levels, attenuating mitochondrial dysfunction, and inhibiting EMT. In addition, CD38-ARM-MSC-EVs seem to show more potentially beneficial effects than MSC-EVs and synergistically enhance the antiaging and anti-PF effects of NMN (Scheme 1).

Targeted therapy is an attractive strategy for enhancing the therapeutic efficacy of drugs. Because of their high biocompatibility and ease of surface manipulation, EVs have been widely used for drug delivery in targeted treatment.[28,29,51] Peptides, scFv, and antibodies have been employed as targeting ligands in engineered EVs.[28,29] In contrast to the low specificity of peptides and the poor permeability of antibodies, scFv is a superior targeting ligand with high specificity and permeability and was selected as the targeting ligand with a sequence reportedly exhibiting high affinity for CD38 antigen.[52] Several methods for anchoring scFv on the surface of EVs have been recently developed,[30−33] such as fusing scFv with the C1C2 structure of lactadhesin and phosphatidylserine (PS);[30,31] however, the transient binding affinity between C1C2 and PS[53] is unstable and even inhibits the EV uptake by target cells.[31] Another method is using transmembrane protein fusion targeting ligands, such as Lamp2b,[54] which may cleave peptide ligands or nullify fusion protein expression.[30] In addition, CAR technology has also been employed to engineer EVs with surface scFv.[37−41] The clinical application of CAR technology inspired us to engineer EVs using the principles of CAR technology, which may have a potential rapid clinical translation value. To construct CD38-ARM-MSC-EVs, we employed the CAR transmembrane domain architecture, which incorporates the CD8 transmembrane region for linking anti-CD38 scFv and EVs without the intracellular stimulatory regions specific for CAR-T or CAR-NK cells[55] but not MSCs. As expected, our results confirmed that CD38-ARM-MSC-EVs specifically bound to $CD38^{high}$ cells. Thus, our study allows the application of scFv to alter stem-cell-derived EVs, thereby offering an encouraging strategy for surface-engineered EVs derived from stem cells.

Aging is a capital factor in repeated respiratory epithelial barrier injury, which contributes to the exacerbation of PF.[17,56,57] Targeting CD38 via drug inhibition or genetic ablation can ameliorate PF by reversing NAD^+ decline.[4,9] In contrast to these existing studies, we used engineered CD38-ARM-MSC-EVs to target senescent AEC2s to demonstrate significant antiaging and anti-PF functions. In addition, we also showed that CD38-ARM-MSC-EVs could increase NAD^+ levels and enhance NAD^+ pathway-related functions that play important roles in cell and body aging (using 78c, a CD38 inhibitor (Figure S6), and NMN, a precursor of NAD^+, as positive controls), which may be attributed to the function of CD38 as the main NADase. MSC-EVs also exhibited these enhanced effects, although they remained significantly and numerically less than CD38-ARM-MSC-EVs in vitro and in vivo, respectively. Interestingly, both types of EV treatments produced different in vitro trends with NMN treatment when age-related and most EMT-related markers were considered. Compared with the EV-treated groups, the NMN-treated group exhibited the weakest antiaging and anti-PF effects but the most significant increase in NAD^+ levels, synthesis, and function-associated genes. The underlying mechanisms may involve the participation of NMN as a precursor of NAD^+, and the added NMN could subsequently directly elevate NAD^+ levels and exert a more prominent influence on NAD^+-related pathways, compared with both EVs; however, umbilical cord MSC-EVs contain multiple youthful bioactive molecules that regulate multiple aging-related functions with powerful antiaging effects[58] and could significantly rejuvenate cell senescence more efficiently than NMN, which only regulates the NAD^+-related pathway.

Numerous studies have assessed the anti-PF effects of EVs in drug-induced models;[24−27] however, only a few have reported that umbilical cord MSC-EVs possess anti-PF effects.[27,59] In this study, we aimed to focus on the anti-PF functions of umbilical cord MSC-EVs in aged mice. Our study supports the

https://doi.org/10.1021/acsnano.3c10547
ACS Nano 2024, 18, 7046−7063

use of not only CD38-ARM-MSC-EVs but also natural umbilical cord MSC-EVs to treat age-related PF. Given the existing strong anti-PF effects of MSC-EVs, our targeted engineering approach may not add significantly more anti-PF functions to them, although more potentially beneficial effects have been shown. On the other hand, the limited amount of both types of EVs in the lung, compared to that in the other $CD38^{high}$ organs, should also be responsible, although the distribution of CD38-ARM-MSC-EVs in the lung was much more than that of MSC-EVs. Importantly, CD38-ARM-MSC-EVs could be used as targeting carriers for drugs against PF or engineered with dual targets of CD38 and SP-A to increase the level of accumulation in the lung and reduce their distribution in other organs. These strategies may help enhance their anti-PF effects with improved safety profiles.

Current anti-PF drugs, such as pirfenidone and nintedanib, primarily focus on fibroblasts and exert their effects through a relatively single-layer mechanism.[2,3] Our study highlights the ability of CD38-ARM-MSC-EVs to selectively target senescent AEC2s and alleviate aging-related PF. Additionally, CD38-ARM-MSC-EVs could elevate NAD^+ levels and potentially amplify the anti-PF effects of NMN. The present study proposes CD38-ARM-MSC-EVs as a prospective anti-PF agent that acts via diverse mechanisms involving cell senescence and cellular energy metabolism and suggests a possible combination anti-PF regimen, thereby indicating a promising clinical translation potential. Furthermore, CD38-ARM-MSC-EVs exhibit the advantage of higher accumulation in aged mice and mitigating multiple age-associated phenotypes, compared with unmodified MSC-EVs, thereby demonstrating promising clinical value in age-related degeneration and diseases. However, more details regarding how CD38-ARM-MSC-EVs rejuvenate cellular senescence by inhibiting CD38 enzyme activity, how they affect senescent AEC2s and other $CD38^{high}$ senescent cells in PF development, and how they cooperate with NMN remain to be elucidated.

Previously, we reported that unmodified umbilical cord MSC-EVs reversed cell senescence and delayed the degeneration of multiple tissues and organs, such as the kidney, blood vessels, and bone, in aged mice;[58] however, we also observed that several mice died following an intravenous injection of MSC-EVs (data not shown), consistent with the findings of a previous report.[60] Therefore, in the present study, we used intraperitoneal injection, a safer method,[61] instead of intravenous injection. Accordingly, CD38-ARM-MSC-EVs exhibited considerably stronger antiaging properties than unmodified MSC-EVs in mitigating multiple age-related phenotypes (see Figures S9 and S10). However, for MSC-EVs, we only observed reduced SA-β-GAL activity and improved renal function, with no obvious changes in organ structures and fiber deposition and formation in the kidney, unlike our previous findings.[58] This was possibly caused by the intraperitoneal injection, which altered the distribution of EVs in vivo and resulted in fewer EVs reaching the kidney (see Figures S7 and S8).

CONCLUSIONS

We developed an effective method to establish surface-engineered MSC-EVs with specific targets. For PF treatment, the CD38-ARM-MSC-EVs may not only serve as a promising biologic drug to be developed with high clinical potential but also be utilized to carry anti-PF drugs with more precise targeting capacities in the future.

METHODS

Cell Culture. At Wuhan Union Hospital, human umbilical cord samples were obtained from consenting donors delivering full-term infants by a cesarean section. MSCs were isolated and characterized as previously described.[62] Newly obtained MSCs were cultured in Dulbecco's modified Eagle's medium (DMEM)/F-12 medium (Gibco) supplemented with 10% fetal bovine serum (FBS; Gibco) and 100 units/mL penicillin/streptomycin at 37 °C in a 5% CO_2 environment. Serial passaging was performed when the cells reached 80%−100% confluence and were still actively dividing. Experimental procedures were conducted using MSCs within ten passages.

The A549, RAW264.7 and RPMI8226 cell lines used in this study were purchased from Pricella, Inc. (China). A549 cells were grown in DMEM/F-12 medium (Gibco) supplemented with 10% FBS (Gibco) and 100 U/mL penicillin/streptomycin (Gibco) at 37 °C in 5% CO_2. RAW264.7 cells were grown in DMEM (Gibco) supplemented with 10% FBS (Gibco) and 100 U/mL penicillin/streptomycin (Gibco) at 37 °C in 5% CO_2. RPMI8226 cells were grown in RPMI-1640 (Gibco) supplemented with 10% FBS (Gibco) and 100 U/mL penicillin/streptomycin (Gibco) at 37 °C in 5% CO_2.

The human BMSCs used in this study were purchased from Cyagen Biosciences, Inc. The aforementioned cells were grown in α-MEM (Gibco) supplemented with 10% FBS (Gibco) and 100 U/mL penicillin/streptomycin (Gibco) at 37 °C in 5% CO_2.

Design and Transfection of CD38-ARM Lentiviral Vectors. In this study, the CD38-ARM construct was encoded by GV401-GFP and contained an anti-CD38 scFv (Table S1),[52] hinge and transmembrane regions from CD8. As a control, the CD38-scFv construct and CD8 transmembrane construct were separately encoded by GV401-GFP. These lentiviruses were synthesized by GeneChem Co., Ltd. With HitransG A transfection reagent, the lentivirus was incubated at a multiplicity of infection of 50 in MSCs (seeded at 4×10^4 cells/cm^2). After 12 h of culture, the viral supernatants were removed, and the cells were washed with PBS. Fresh medium was added, and the transfected cells were cultured for an additional 60 h. The transduction efficiency of CD38-ARM was subsequently confirmed through qPCR and flow cytometry. After transduction, the cells were cultured in a manner similar to that used for the MSCs.

Generation and Isolation of EVs. According to previous publications, MSC and engineered MSC supernatants were used for EV isolation.[58,62] The culture medium underwent a series of centrifugation steps to isolate the EVs. Initially, the medium was centrifuged at 750*g* for 15 min to eliminate cells, followed by centrifugation at 2000*g* for 20 min at 4 °C to remove apoptotic bodies and debris. Subsequently, the supernatant was subjected to further centrifugation at 16 000*g* (Avanti J-26S XPI High-Performance Centrifuge; Beckman Coulter, Brea, CA, USA) for 60 min at 4 °C to pelletize the EVs. After washing and resuspension in sterile PBS, the EVs were either used immediately or stored frozen at −80 °C until needed. The number of MSC-EVs and CD38-ARM-MSC-EVs obtained was determined by lysing purified EV particles in RIPA buffer and quantifying the total protein content via a BCA protein assay.

Nanoparticle Tracking Analysis (NTA). The dimensions and density of the MSC-EVs and CD38-ARM-MSC-EVs were assessed via NTA using the ZetaView platform (Particle Metrix, Meerbusch, Germany). MSC-EVs and CD38-ARM-MSC-EVs were suitably diluted with PBS and subsequently evaluated at room temperature. The scattered dots were amplified by a factor of 10 to capture an image of the EVs to monitor Brownian motion.

Transmission Electron Microscopy. Ten microliters of MSC-EVs and CD38-ARM-MSC-EVs were deposited onto a 200-mesh copper grid for a duration of 2 min and gently dried by blotting with filter paper. Next, the grids were stained with 10 microliters μL of 2% uranyl acetate in the absence of light for a period of 3 min. Ultimately, the grids were visualized via transmission electron microscopy (TEM) (Model HT7800, Hitachi, Tokyo, Japan) at 80.0 kV.

https://doi.org/10.1021/acsnano.3c10547
ACS Nano 2024, 18, 7046−7063

Flow Cytometry. The flow cytometry of EVs was performed by using a flow cytometry instrument (ID7000, Sony). To define an EV gate, fluorescent submicrometer beads with diameters of 0.2, 0.5, and 0.76 μm (Bangs Laboratories, Inc.) were utilized. In our experiment, EVs that were purified were identified as events gated with diameters of <0.76 μm. To characterize the immunophenotypes of MSC-EVs and CD38-ARM-MSC-EVs, EVs were incubated with antihuman CD73, CD90, CD105, and isotype control antibodies for 20 min.

ARM expression was detected using biotinylated recombinant protein CD38 (ACROBiosystems) at a concentration of 100 ng/10^6 cells or 100 ng/10 μg EVs. The samples underwent incubation with biotinylated recombinant CD38 protein, followed by incubation with PE-conjugated streptavidin (ACROBiosystems), to ascertain the proportion of CD38-ARM−positive MSCs and CD38-ARM−positive EVs. The data were subsequently analyzed via FlowJo software (Tree Star Inc., Ashland, OR, USA).

We incubated MSCs and engineered MSCs with antihuman CD29, CD44, CD73, CD90, CD105, CD31, CD34, and CD45 antibodies for 20 min before analysis with a FACSCalibur (BD Biosciences).

A549 cells treated with or without DOX, RPMI8226 cells, and BMSCs were incubated with antihuman CD38 antibody for 20 min, as well as RAW264.7 cells treated with or without LPS were incubated with antimouse CD38 antibody for 20 min; and then analyzed with a FACSCalibur (BD Biosciences).

Western Blot Analysis. Cells or EVs were subjected to lysis in ice-cold RIPA buffer (Beyotime) at 4 °C for 30 min. Subsequently, lysates containing 25 μg of protein were subjected to analysis via 10% sodium dodecyl sulfate−polyacrylamide gel electrophoresis (Sigma−Aldrich) and transferred onto nitrocellulose membranes (Merck Millipore, Billerica, MA, USA). These membranes were then subjected to hybridization with antibodies against CD38, CD9, CD63, CD81, TSG101, GFP, or β-actin. Finally, the membranes were incubated with HRP-conjugated secondary antibodies.

Quantitative Real-Time PCR (qPCR). The RNA Easy Isolation Reagent (Vazyme, China) was used to extract total RNA from MSCs. A ReverTra Ace qPCR RT Kit (TOYOBO) was employed for the reverse transcription of RNA samples from MSCs. The StepOnePlus Real-Time PCR System (Thermo Fisher Scientific, Inc.) was utilized for qPCR with the SYBR Green PCR master mix. The primer sequences are listed in Table S2.

Enzyme-Linked Immunosorbent Assay (ELISA). The levels of SASP factors, including IL-1β, IL-6, TNF-α, and MCP-1, and profibrotic factors, including TGF-β, MMP2, and MMP9, were quantified via ELISAs using commercially available kits (Bio-Swamp).

Uptake of EVs by Cells In Vitro. A PKH26 Red Fluorescent Cell Linker Kit for General Cell Membrane Labeling (Sigma−Aldrich) was used to stain purified MSC-EVs and CD38-ARM-MSC-EVs.[63] Cells (including RAW264.7 cells treated with or without LPS and A549 cells treated with or without DOX) were seeded into 12-well plates and incubated with PKH26-labeled EVs at 37 °C for 2 h. After PBS washes, the cells were fixed with 4% formaldehyde for 10 min at room temperature. Then, the cells were rinsed, stained with DAPI for 10 min at room temperature, and visualized using a fluorescence microscope.

For determination of the cellular uptake efficiency of PKH26-labeled EVs by RPMI8226 cells and BMSCs, 1 × 10^5 RPMI8226 cells stained with carboxyfluorescein diacetate succinimidyl ester (CSFE) (Solarbio) were seeded in each well of a 12-well plate containing 2 × 10^4 BMSCs/well (added to the plates 24 h before RPMI8226 cell application). These cells were incubated with PKH26-labeled EVs at 37 °C for 24 h. The medium containing RPMI8226 cells (suspension cells) was collected, and the BMSCs (adherent cells) in the plates were rinsed and stained with DAPI. Finally, both RPMI8226 cells and BMSCs were imaged using a fluorescence microscope and analyzed by ImageJ software (NIH).

For further analysis of the ability of CD38-ARM-MSC-EVs to bind to the surface CD38 antigen on $CD38^{high}$ A549 cells, 1 × 10^5 A549 cells, pretreated with 0.25 μM DOX for 48 h, were treated with 2 μg/mL daratumumab (Selleck) to block cell surface CD38 for 3 h, and followed by incubation with PKH26-labeled CD38-ARM-MSC-EVs or MSC-EVs for another 2 h. After fixation with 4% formaldehyde for 10 min at room temperature, the cells were rinsed, stained with DAPI for 10 min at room temperature, and visualized using a fluorescence microscope.

In Vitro Senescent AEC2 Model. A549 cells were stimulated with DOX for 2 days to establish the senescent AEC2 model. A549 cells were seeded overnight in 6-well culture plates at a density of 1 × 10^5 cells/cm^2. Then, the A549 cells were treated with DOX (0, 0.125, 0.25, or 0.5 μM). After stimulation for 48 h, the medium containing DOX was removed, and fresh medium was added to the cells for starvation for 24 h. Several aging-related markers, including cellular morphology, cell viability, SA-β-Gal, and SASP, were tested to confirm the senescent state of these cells.

Cell Viability Analysis. Cell viability was evaluated using the CCK-8 kit (Vazyme), according to the manufacturer's instructions. Briefly, cells were seeded at an appropriate number in 96-well plates in triplicate and incubated at 37 °C for 24, 48, or 72 h. Following the addition of 10 μL of the CCK-8 reagent, the cells were incubated for an additional 2 h. The absorbance was measured on a microplate reader (PerkinElmer EnSpire, Waltham, MA, USA) at 450 nm.

EV Treatment In Vitro. Initially, 1 × 10^5 A549 cells/cm^2 were cultured in 6-well plates and were stimulated with DOX (0.25 μM) for 48 h. The medium containing DOX was removed, the cells were washed three times with PBS, and fresh medium was added. Then, the cells were separately treated with MSC-EVs (10 μg/mL), CD38-ARM-MSC-EVs (10 μg/mL), NMN (0.5 mM, Macklin), NMN + MSC-EVs, and NMN + CD38-ARM-MSC-EVs, or an equal volume of PBS (as a control) once a day. After 2 days, the cells were collected for further testing.

Similarly, A549 cells were stimulated with DOX (0.25 μM) for 2 days to establish a senescent AEC2 model. After the cells were washed with PBS, fresh medium was added. The cells were separately treated with MSC-EVs (10 μg/mL), CD38-ARM-MSC-EVs (10 μg/mL), 78c (0.5 μM, Selleck), 78c + MSC-EVs, 78c + CD38-ARM-MSC-EVs, or an equal volume of PBS (as a control) once a day. After 2 days, the cells were collected for further analysis of their NAD^+ concentration.

SA-β-Gal Staining Assay. A549 cells were fixed in fixative solution for 30 min, stained with SA-β-Gal staining solution (Beyotime), and incubated overnight at 37 °C. The SA-β-Gal-positive cells were visualized with a microscope (Olympus) and quantified with ImageJ software (NIH).

Mouse lung tissues were obtained for OCT frozen sections (~10 μm) and processed with a Senescence Detection Kit (Abcam, ab65351), according to the manufacturer's instructions.

Osteogenic Differentiation. MSCs were cultured in 6-well plates (4 × 10^4 cells/well) and induced to differentiate into osteoblasts by applying osteogenic induction medium (Cyagen Biosciences, Inc.). At 21 days post-induction, Alizarin Red S (Beyotime) was utilized to stain the cells at pH 4.2 to evaluate mineralization of the cell matrix.

Adipogenic Differentiation. We induced MSC adipogenic differentiation in vitro, as previously described.[58,61] MSCs were cultured in adipogenic induction medium (Cyagen Biosciences, Inc.) in six-well plates (8 × 10^4 cells/well) for 14 days. The cells were stained with an Oil Red O solution (Beyotime) to distinguish mature adipocytes from preadipocytes.

ROS Detection. DOX-stimulated A549 cells were incubated with PBS, MSC-EVs, CD38-ARM-MSC-EVs, NMN, NMN + MSC-EVs or NMN + CD38-ARM-MSC-EVs for 48 h. At the indicated time points, the media were removed, and 500 μL of 2′,7′-dichlorodihydrofluorescein (DCFH-DA) (Beyotime) solution (10 μM) was added to each well and coincubated for 30 min at 37 °C. After three gentle rinses with PBS, the intracellular ROS level was evaluated by observing the green signal fluorescence of 2′,7′-dichlorofluorescein (DCF) via an inverted fluorescence microscope (Olympus).

Measurement of Mitochondrial Transmembrane Potential. A JC-1 mitochondrial membrane potential assay kit (Beyotime) was used to evaluate the mitochondrial membrane potential. DOX-stimulated A549 cells were incubated with PBS, MSC-EVs, CD38-ARM-MSC-EVs, NMN, NMN + MSC-EVs or NMN + CD38-ARM-

https://doi.org/10.1021/acsnano.3c10547
ACS Nano 2024, 18, 7046−7063

MSC-EVs for 48 h. At the indicated time points, the cells were washed with PBS once and incubated with 500 μL of staining working buffer per well for 20 min at 37 °C, after which the covering liquid was changed to DMEM/F12 after the cells were washed with staining buffer solution twice. The mitochondrial transmembrane potential was evaluated by observing the green signal fluorescence of the JC-1 monomers and the red signal fluorescence of the JC-1 aggregates via an inverted fluorescence microscope (Olympus).

Small RNA Sequencing and Analysis. MSC-EVs and CD38-ARM-MSC-EV RNA were isolated using Qiagen's QIAseq miRNA Library Kit. Once the RNA was isolated, it was further analyzed by sequencing. The RNA purity was assessed using a NanoPhotometer spectrophotometer (IMPLEN, Westlake Village, CA, USA). The RNA concentration was measured using a Qubit RNA Assay Kit in a Qubit 2.0 Fluorometer (Life Technologies, Carlsbad, CA, USA). RNA integrity was assessed using the RNA Nano 6000 Assay Kit of the Agilent Bioanalyzer 2100 system (Agilent Technologies, Santa Clara, CA, USA). Small RNA sequencing libraries were generated using the NEBNext Multiplex Small RNA Library Prep Set for Illumina (NEB, Ipswich, MA, USA), following the manufacturer's recommendations. The library quality was assessed on an Agilent Bioanalyzer 2100 system using DNA High Sensitivity Chips. Clustering of the index-coded samples was performed on a cBot Cluster Generation System using TruSeq SR Cluster Kit v3-cBot-HS (Illumina, San Diego, CA, USA) according to the manufacturer's instructions. After cluster generation, the library preparations were sequenced on an Illumina HiSeq 2500/2000 platform and 50 bp single-end reads were generated.

Mice. The animal experimental protocols were conducted according to the Guide for the Care and Use of Laboratory Animals of the National Institutes of Health and were approved by the Institutional Animal Care and Use Committee of Tongji Medical College, Huazhong University of Science and Technology (No. 2022012). Male C57BL/6J mice (2−3 months old) were purchased from Shulaibao (Wuhan) Biotechnology Co., Ltd. Male C57BL/6J mice (16−21 months old) were purchased from Wuhan Youdu Biotechnology Co., Ltd. The mice were randomly divided into different groups and housed under pathogen-free conditions. A standard chow diet was given to all mice ad libitum, and the mice were kept on a 12-h light/12-h dark cycle. We monitored the health status of the mice periodically, and no obvious behavioral differences were observed.

Biodistribution of EVs In Vivo. One hundred micrograms (100 μg) of EVs were stained with DiR fluorescent dye (Rengen Biosciences) for imaging with an Image System Lago/Lago X imaging system (Spectral Instruments Imaging, Tucson, AZ, USA). The MSC-EVs or CD38-ARM-MSC-EVs were incubated with 15 mM dye at 37 °C in darkness for 30 min. After two washes with PBS, both types of EVs were resuspended in 100 μL of PBS and intraperitoneally administered to 18-month-old C57BL/6J mice. Two hours after injection, the mice were harvested, and their major organs were imaged ex vivo using the Image System Lago/Lago X imaging system.

One hundred micrograms (100 μg) of EVs were labeled with PKH26 and intraperitoneally administered to 18-month-old C57BL/6J mice. At 2 h post-injection, the extracted major tissues, including the lung, liver, heart, spleen, and kidney, were snap-frozen and sectioned at 5 mm. The senescent cells in the lung were stained with a mouse anti-CD38 antibody or a mouse anti-SP-A antibody, and the cell nuclei were labeled via DAPI staining. Slides were imaged and documented using an inverted fluorescence microscope camera system (Olympus).

A total of 150 μg of EVs were stained with DiR fluorescent dye for imaging with an Image System Lago/Lago X imaging system. DiR-labeled EVs were intraperitoneally administered to young (2 months old) and old (21 months old) C57BL/6J mice. The mice were harvested after 24 h of intraperitoneal delivery, and their major organs were imaged ex vivo, using the Image System Lago/Lago X imaging system. Once imaged, all tissues were collected and cryopreserved in OCT for further characterization.

In Vivo Antiaging Effects. For further analysis of the effects of NMN and EVs on the degeneration of various tissue organs in naturally aged mice, 17-month-old C57BL/6J mice were randomly divided into six groups: the PBS group, the MSC-EV group, the CD38-ARM-MSC-EV group, the NMN group, the NMN + CD38-ARM-MSC-EV group, and the NMN + MSC-EV group. Mice in the PBS group were injected with 200 μL of PBS every day. The mice in the NMN group, NMN + MSC-EV group, and NMN + CD38-ARM-MSC-EV group were injected with 500 mg/kg NMN every day. The mice in the MSC-EV, CD38-ARM-MSC-EV, NMN + MSC-EV and NMN + CD38-ARM-MSC-EV groups were injected with 60 μg of EVs every 2 days for 4 weeks. The body weights of the mice were measured weekly, and on the 29th day, the mice were sacrificed. Approximately 500−1000 μL of blood was collected from each mouse. The organs were collected to be prepared in frozen sections and paraffin sections.

Histological and Immunohistochemical (IHC) Analysis. Staining with hematoxylin and eosin (H&E) and Masson's trichrome was performed as previously described.[58] For IHC staining, lung tissue sections were incubated with p21, *α-SMA*, and *E-cad* antibodies, followed by a blocking step at 37 °C with goat serum. After the sections were stained with primary antibodies, they were incubated for 1 h with secondary antibodies conjugated to horseradish peroxidase (HRP). After washing in PBS, the slides were subjected to HRP-DAB chromogenic staining. The antibody information is displayed in Table S3.

NAD^+, NADP, and Other Metabolite Measurements. The NAD^+ content in A549 cells in vitro was measured using the NAD Assay Kit (from Beyotime), according to the manufacturer's protocol.

The NAD^+, NADP, and NAM content in the lung tissue of the mice was measured by HPLC-MS. After the addition of 500 μL of extraction solvent (precooled at −20 °C, acetonitrile−methanol−water, 2:2:1), the samples were vortexed for 30 s, homogenized at 38 Hz for 4 min, and sonicated for 5 min in an ice−water bath, followed by incubation at −20 °C for 1 h and centrifugation at 12 000 rpm and 4 °C for 15 min. Fifty microliters (50 μL) of the supernatant was diluted 5 and 100 times for HPLC-MS analysis. Mobile phase A was ammonium bicarbonate in water, and mobile phase B was acetonitrile. The elution gradient is shown in Table S4. The flow rate was 300 μL/min. The column temperature was set at 35 °C. The autosampler temperature was set at 10 °C, and the injection volume was 1 μL.

Statistical Analysis. One-way analysis of variance (ANOVA), two-way ANOVA, and Student's *t*-test were performed utilizing GraphPad Prism 9.0 software (GraphPad software, La Jolla, CA, USA) to analyze the data. All the data are presented as the means ± standard deviations. $P < 0.05$ was considered to indicate statistical significance.

ASSOCIATED CONTENT

Data Availability Statement

The small RNA-seq data are available at the BIGD Genome Sequence Archive (GSA), under Accession No. PRICA020632.

Supporting Information

The Supporting Information is available free of charge at https://pubs.acs.org/doi/10.1021/acsnano.3c10547.

Supplementary figures with data that further support conclusions made in the main document; supplementary tables listing information about sequence alignment of anti-CD38 scFv, primer sequences of qPCR, list of antibodies, and liquid chromatography gradient (PDF)

AUTHOR INFORMATION

Corresponding Authors

Zhichao Chen − *Department of Hematology, Union Hospital, Tongji Medical College, Huazhong University of Science and*

https://doi.org/10.1021/acsnano.3c10547
ACS Nano 2024, 18, 7046−7063

Technology, Wuhan 430022, China; Email: chenzhichao@hust.edu.cn

Qiubai Li − *Department of Rheumatology and Immunology, Union Hospital, Tongji Medical College, Huazhong University of Science and Technology, Wuhan 430022, China; Hubei Engineering Research Center for Application of Extracellular Vesicle, Hubei University of Science and Technology, Xianning 437100, China;* orcid.org/0000-0001-7884-0745; Email: qiubaili@hust.edu.cn

Authors

Yaoying Long − *Department of Hematology, Union Hospital, Tongji Medical College, Huazhong University of Science and Technology, Wuhan 430022, China;* orcid.org/0000-0003-4517-1375

Bianlei Yang − *Department of Rheumatology and Immunology, Union Hospital, Tongji Medical College, Huazhong University of Science and Technology, Wuhan 430022, China*

Qian Lei − *West China Biomedical Big Data Center, West China Hospital, Sichuan University, Chengdu 610041, China*

Fei Gao − *Department of Hematology, The Central Hospital of Wuhan, Tongji Medical College, Huazhong University of Science and Technology, Wuhan 430014, China*

Li Chen − *Department of Hematology, The Central Hospital of Wuhan, Tongji Medical College, Huazhong University of Science and Technology, Wuhan 430014, China*

Wenlan Chen − *Department of Hematology, Union Hospital, Tongji Medical College, Huazhong University of Science and Technology, Wuhan 430022, China*

Siyi Chen − *Department of Rheumatology and Immunology, Union Hospital, Tongji Medical College, Huazhong University of Science and Technology, Wuhan 430022, China*

Wenxiang Ren − *Department of Hematology, Union Hospital, Tongji Medical College, Huazhong University of Science and Technology, Wuhan 430022, China*

Yulin Cao − *Department of Rheumatology and Immunology, Union Hospital, Tongji Medical College, Huazhong University of Science and Technology, Wuhan 430022, China*

Liuyue Xu − *Department of Hematology, Union Hospital, Tongji Medical College, Huazhong University of Science and Technology, Wuhan 430022, China*

Di Wu − *Department of Hematology, Union Hospital, Tongji Medical College, Huazhong University of Science and Technology, Wuhan 430022, China*

Jiao Qu − *Department of Hematology, Union Hospital, Tongji Medical College, Huazhong University of Science and Technology, Wuhan 430022, China*

He Li − *Department of Hematology, Union Hospital, Tongji Medical College, Huazhong University of Science and Technology, Wuhan 430022, China*

Yali Yu − *Department of Rheumatology and Immunology, Union Hospital, Tongji Medical College, Huazhong University of Science and Technology, Wuhan 430022, China*

Anyuan Zhang − *Department of Hematology, Union Hospital, Tongji Medical College, Huazhong University of Science and Technology, Wuhan 430022, China*

Shan Wang − *Department of Hematology, Union Hospital, Tongji Medical College, Huazhong University of Science and Technology, Wuhan 430022, China*

Weiqun Chen − *Key Laboratory for Molecular Diagnosis of Hubei Province, The Central Hospital of Wuhan, Tongji Medical College, Huazhong University of Science and Technology, Wuhan 430014, China*

Hongxiang Wang − *Department of Hematology, The Central Hospital of Wuhan, Tongji Medical College, Huazhong University of Science and Technology, Wuhan 430014, China*

Ting Chen − *Hubei Engineering Research Center for Application of Extracellular Vesicle, Hubei University of Science and Technology, Xianning 437100, China*

Complete contact information is available at: https://pubs.acs.org/10.1021/acsnano.3c10547

Author Contributions

[▽]Y. Long and B. Yang contributed equally to this work. C.Z. and L.Q. designed the research. L.Y. and Y.B. conducted the experiments and analyzed the data. L.Q., G.F., C.L., and C.W. assisted in the transfection of CD38-specific ARM lentiviral vectors. C.S., R.W., C.Y., and X.L. assisted in the cell culture experiments and EV collection. W.D., Q.J., L.H., Y.Y., Z.A., and W.S. performed the animal experiments. C.W., W.H., and C.T. assisted in image processing. L.Y., Y.B., C.Z., and L.Q. wrote the manuscript. All authors have approved the submitted version of the manuscript.

Notes

The authors declare no competing financial interest.

ACKNOWLEDGMENTS

This work was financially supported by the National Key R&D Program of China (No. 2021YFA1101500), the National Natural Science Foundation of China (Grant Nos. 81974221, 81974009, and 92049119), the Hubei Innovation Group Foundation (No. 2022CFA019), and the Project of Wuhan Municipal Health Commission (No. WX21A15). We would like to thank the engineer Wang Jia (from Shanghai Bioprofile Technology Company Ltd., China) for help with the small RNA analysis.

REFERENCES

(1) Richeldi, L.; Collard, H. R.; Jones, M. G. Idiopathic pulmonary fibrosis. *Lancet* **2017**, *389* (10082), 1941−1952.

(2) Behr, J.; Prasse, A.; Kreuter, M.; Johow, J.; Rabe, K. F.; Bonella, F.; Bonnet, R.; Grohe, C.; Held, M.; Wilkens, H.; et al. Pirfenidone in patients with progressive fibrotic interstitial lung diseases other than idiopathic pulmonary fibrosis (RELIEF): a double-blind, randomised, placebo-controlled, phase 2b trial. *Lancet Respir. Med.* **2021**, *9* (5), 476−486.

(3) Umemura, Y.; Mitsuyama, Y.; Minami, K.; Nishida, T.; Watanabe, A.; Okada, N.; Yamakawa, K.; Nochioka, K.; Fujimi, S. Efficacy and safety of nintedanib for pulmonary fibrosis in severe pneumonia induced by COVID-19: An interventional study. *Int. J. Infect. Dis.* **2021**, *108*, 454−460.

(4) Camacho-Pereira, J.; Tarrago, M. G.; Chini, C. C. S.; Nin, V.; Escande, C.; Warner, G. M.; Puranik, A. S.; Schoon, R. A.; Reid, J. M.; Galina, A.; et al. CD38 Dictates Age-Related NAD Decline and Mitochondrial Dysfunction through an SIRT3-Dependent Mechanism. *Cell Metab.* **2016**, *23* (6), 1127−1139.

(5) Chini, C. C. S.; Peclat, T. R.; Warner, G. M.; Kashyap, S.; Espindola-Netto, J. M.; de Oliveira, G. C.; Gomez, L. S.; Hogan, K. A.; Tarrago, M. G.; Puranik, A. S.; et al. CD38 ecto-enzyme in immune cells is induced during aging and regulates NAD(+) and NMN levels. *Nat. Metab.* **2020**, *2* (11), 1284−1304.

(6) Chini, E. N.; Chini, C. C. S.; Espindola Netto, J. M.; de Oliveira, G. C.; van Schooten, W. The Pharmacology of CD38/NADase: An Emerging Target in Cancer and Diseases of Aging. *Trends Pharmacol. Sci.* **2018**, *39* (4), 424−436.

(7) Gomes, A. P.; Price, N. L.; Ling, A. J.; Moslehi, J. J.; Montgomery, M. K.; Rajman, L.; White, J. P.; Teodoro, J. S.; Wrann, C. D.; Hubbard, B. P.; et al. Declining NAD(+) induces a pseudohypoxic state disrupting nuclear-mitochondrial communication during aging. *Cell* **2013**, *155* (7), 1624−1638.
(8) Covarrubias, A. J.; Perrone, R.; Grozio, A.; Verdin, E. NAD(+) metabolism and its roles in cellular processes during ageing. *Nat. Rev. Mol. Cell Biol.* **2021**, *22* (2), 119−141.
(9) Tarrago, M. G.; Chini, C. C. S.; Kanamori, K. S.; Warner, G. M.; Caride, A.; de Oliveira, G. C.; Rud, M.; Samani, A.; Hein, K. Z.; Huang, R.; et al. A Potent and Specific CD38 Inhibitor Ameliorates Age-Related Metabolic Dysfunction by Reversing Tissue NAD(+) Decline. *Cell Metab.* **2018**, *27* (5), 1081−1095.e10.
(10) Yoshino, M.; Yoshino, J.; Kayser, B. D.; Patti, G. J.; Franczyk, M. P.; Mills, K. F.; Sindelar, M.; Pietka, T.; Patterson, B. W.; Imai, S. I.; et al. Nicotinamide mononucleotide increases muscle insulin sensitivity in prediabetic women. *Science* **2021**, *372* (6547), 1224−1229.
(11) Nadeeshani, H.; Li, J.; Ying, T.; Zhang, B.; Lu, J. Nicotinamide mononucleotide (NMN) as an anti-aging health product - Promises and safety concerns. *J. Adv. Res.* **2022**, *37*, 267−278.
(12) Cui, H.; Xie, N.; Banerjee, S.; Dey, T.; Liu, R. M.; Antony, V. B.; Sanders, Y. Y.; Adams, T. S.; Gomez, J. L.; Thannickal, V. J.; et al. CD38 Mediates Lung Fibrosis by Promoting Alveolar Epithelial Cell Aging. *Am. J. Respir. Crit. Care Med.* **2022**, *206* (4), 459−475.
(13) Desai, T. J.; Brownfield, D. G.; Krasnow, M. A. Alveolar progenitor and stem cells in lung development, renewal and cancer. *Nature* **2014**, *507* (7491), 190−194.
(14) Pineiro-Hermida, S.; Martinez, P.; Bosso, G.; Flores, J. M.; Saraswati, S.; Connor, J.; Lemaire, R.; Blasco, M. A. Consequences of telomere dysfunction in fibroblasts, club and basal cells for lung fibrosis development. *Nat. Commun.* **2022**, *13* (1), 5656.
(15) Parimon, T.; Yao, C.; Stripp, B. R.; Noble, P. W.; Chen, P. Alveolar Epithelial Type II Cells as Drivers of Lung Fibrosis in Idiopathic Pulmonary Fibrosis. *Int. J. Mol. Sci.* **2020**, *21* (7), 2269.
(16) Yao, C.; Guan, X.; Carraro, G.; Parimon, T.; Liu, X.; Huang, G.; Mulay, A.; Soukiasian, H. J.; David, G.; Weigt, S. S.; et al. Senescence of Alveolar Type 2 Cells Drives Progressive Pulmonary Fibrosis. *Am. J. Respir. Crit. Care Med.* **2021**, *203* (6), 707−717.
(17) Selman, M.; Pardo, A. Revealing the pathogenic and aging-related mechanisms of the enigmatic idiopathic pulmonary fibrosis. an integral model. *Am. J. Respir. Crit. Care Med.* **2014**, *189* (10), 1161−1172.
(18) Fang, T.; Yang, J.; Liu, L.; Xiao, H.; Wei, X. Nicotinamide mononucleotide ameliorates senescence in alveolar epithelial cells. *MedComm (2020)* **2021**, *2* (2), 279−287.
(19) Gan, L.; Liu, D.; Liu, J.; Chen, E.; Chen, C.; Liu, L.; Hu, H.; Guan, X.; Ma, W.; Zhang, Y.; et al. CD38 deficiency alleviates Ang II-induced vascular remodeling by inhibiting small extracellular vesicle-mediated vascular smooth muscle cell senescence in mice. *Signal Transduct. Target Ther.* **2021**, *6* (1), 223.
(20) Mills, K. F.; Yoshida, S.; Stein, L. R.; Grozio, A.; Kubota, S.; Sasaki, Y.; Redpath, P.; Migaud, M. E.; Apte, R. S.; Uchida, K.; et al. Long-Term Administration of Nicotinamide Mononucleotide Mitigates Age-Associated Physiological Decline in Mice. *Cell Metab* **2016**, *24* (6), 795−806.
(21) Yoshino, J.; Mills, K. F.; Yoon, M. J.; Imai, S. Nicotinamide mononucleotide, a key NAD(+) intermediate, treats the pathophysiology of diet- and age-induced diabetes in mice. *Cell Metab.* **2011**, *14* (4), 528−536.
(22) Antes, T. J.; Middleton, R. C.; Luther, K. M.; Ijichi, T.; Peck, K. A.; Liu, W. J.; Valle, J.; Echavez, A. K.; Marban, E. Targeting extracellular vesicles to injured tissue using membrane cloaking and surface display. *J. Nanobiotechnol.* **2018**, *16* (1), 61.
(23) Teng, F.; Fussenegger, M. Shedding Light on Extracellular Vesicle Biogenesis and Bioengineering. *Adv. Sci. (Weinheim)* **2021**, *8* (1), No. 2003505.
(24) Sengupta, V.; Sengupta, S.; Lazo, A.; Woods, P.; Nolan, A.; Bremer, N. Exosomes Derived from Bone Marrow Mesenchymal Stem Cells as Treatment for Severe COVID-19. *Stem Cells Dev.* **2020**, *29* (12), 747−754.
(25) Kadota, T.; Fujita, Y.; Araya, J.; Watanabe, N.; Fujimoto, S.; Kawamoto, H.; Minagawa, S.; Hara, H.; Ohtsuka, T.; Yamamoto, Y.; et al. Human bronchial epithelial cell-derived extracellular vesicle therapy for pulmonary fibrosis via inhibition of TGF-beta-WNT crosstalk. *J. Extracell. Vesicles* **2021**, *10* (10), No. e12124.
(26) Dinh, P. C.; Paudel, D.; Brochu, H.; Popowski, K. D.; Gracieux, M. C.; Cores, J.; Huang, K.; Hensley, M. T.; Harrell, E.; Vandergriff, A. C.; et al. Inhalation of lung spheroid cell secretome and exosomes promotes lung repair in pulmonary fibrosis. *Nat. Commun.* **2020**, *11* (1), 1064.
(27) Shi, L.; Ren, J.; Li, J.; Wang, D.; Wang, Y.; Qin, T.; Li, X.; Zhang, G.; Li, C.; Wang, Y. Extracellular vesicles derived from umbilical cord mesenchymal stromal cells alleviate pulmonary fibrosis by means of transforming growth factor-beta signaling inhibition. *Stem Cell Res. Ther.* **2021**, *12* (1), 230.
(28) Jayasinghe, M. K.; Pirisinu, M.; Yang, Y.; Peng, B.; Pham, T. T.; Lee, C. Y.; Tan, M.; Vu, L. T.; Dang, X. T.; Pham, T. C.; et al. Surface-engineered extracellular vesicles for targeted delivery of therapeutic RNAs and peptides for cancer therapy. *Theranostics* **2022**, *12* (7), 3288−3315.
(29) Richter, M.; Vader, P.; Fuhrmann, G. Approaches to surface engineering of extracellular vesicles. *Adv. Drug Deliv. Rev.* **2021**, *173*, 416−426.
(30) Wang, J. H.; Forterre, A. V.; Zhao, J.; Frimannsson, D. O.; Delcayre, A.; Antes, T. J.; Efron, B.; Jeffrey, S. S.; Pegram, M. D.; Matin, A. C. Anti-HER2 scFv-Directed Extracellular Vesicle-Mediated mRNA-Based Gene Delivery Inhibits Growth of HER2-Positive Human Breast Tumor Xenografts by Prodrug Activation. *Mol. Cancer Ther.* **2018**, *17* (5), 1133−1142.
(31) Longatti, A.; Schindler, C.; Collinson, A.; Jenkinson, L.; Matthews, C.; Fitzpatrick, L.; Blundy, M.; Minter, R.; Vaughan, T.; Shaw, M.; et al. High affinity single-chain variable fragments are specific and versatile targeting motifs for extracellular vesicles. *Nanoscale* **2018**, *10* (29), 14230−14244.
(32) Zou, X.; Yuan, M.; Zhang, T.; Wei, H.; Xu, S.; Jiang, N.; Zheng, N.; Wu, Z. Extracellular vesicles expressing a single-chain variable fragment of an HIV-1 specific antibody selectively target Env(+) tissues. *Theranostics* **2019**, *9* (19), 5657−5671.
(33) Ferrantelli, F.; Arenaccio, C.; Manfredi, F.; Olivetta, E.; Chiozzini, C.; Leone, P.; Percario, Z.; Ascione, A.; Flego, M.; Di Bonito, P.; et al. The Intracellular Delivery Of Anti-HPV16 E7 scFvs Through Engineered Extracellular Vesicles Inhibits The Proliferation Of HPV-Infected Cells. *Int. J. Nanomed.* **2019**, *14*, 8755−8768.
(34) Larson, R. C.; Maus, M. V. Recent advances and discoveries in the mechanisms and functions of CAR T cells. *Nat. Rev. Cancer* **2021**, *21* (3), 145−161.
(35) Amor, C.; Feucht, J.; Leibold, J.; Ho, Y. J.; Zhu, C.; Alonso-Curbelo, D.; Mansilla-Soto, J.; Boyer, J. A.; Li, X.; Giavridis, T.; et al. Senolytic CAR T cells reverse senescence-associated pathologies. *Nature* **2020**, *583* (7814), 127−132.
(36) Yang, D.; Sun, B.; Li, S.; Wei, W.; Liu, X.; Cui, X.; Zhang, X.; Liu, N.; Yan, L.; Deng, Y.; et al. NKG2D-CAR T cells eliminate senescent cells in aged mice and nonhuman primates. *Sci. Transl. Med.* **2023**, *15* (709), No. eadd1951.
(37) Zhu, T.; Chen, Z.; Jiang, G.; Huang, X. Sequential Targeting Hybrid Nanovesicles Composed of Chimeric Antigen Receptor T-Cell-Derived Exosomes and Liposomes for Enhanced Cancer Immunochemotherapy. *ACS Nano* **2023**, *17* (17), 16770−16786.
(38) Fu, W.; Lei, C.; Liu, S.; Cui, Y.; Wang, C.; Qian, K.; Li, T.; Shen, Y.; Fan, X.; Lin, F.; et al. CAR exosomes derived from effector CAR-T cells have potent antitumour effects and low toxicity. *Nat. Commun.* **2019**, *10* (1), 4355.
(39) Xu, Q.; Zhang, Z.; Zhao, L.; Qin, Y.; Cai, H.; Geng, Z.; Zhu, X.; Zhang, W.; Zhang, Y.; Tan, J.; et al. Tropism-facilitated delivery of CRISPR/Cas9 system with chimeric antigen receptor-extracellular vesicles against B-cell malignancies. *J. Controlled Release* **2020**, *326*, 455−467.

https://doi.org/10.1021/acsnano.3c10547
ACS Nano 2024, 18, 7046−7063

(40) Yang, P.; Cao, X.; Cai, H.; Feng, P.; Chen, X.; Zhu, Y.; Yang, Y.; An, W.; Yang, Y.; Jie, J. The exosomes derived from CAR-T cell efficiently target mesothelin and reduce triple-negative breast cancer growth. *Cell Immunol.* **2021**, *360*, No. 104262.
(41) Haque, S.; Vaiselbuh, S. R. CD19 Chimeric Antigen Receptor-Exosome Targets CD19 Positive B-lineage Acute Lymphocytic Leukemia and Induces Cytotoxicity. *Cancers (Basel)* **2021**, *13* (6), 1401.
(42) Xu, C.; Hou, L.; Zhao, J.; Wang, Y.; Jiang, F.; Jiang, Q.; Zhu, Z.; Tian, L. Exosomal let-7i-5p from three-dimensional cultured human umbilical cord mesenchymal stem cells inhibits fibroblast activation in silicosis through targeting TGFBR1. *Ecotoxicol. Environ. Saf.* **2022**, *233*, No. 113302.
(43) Zhao, W.; Cheng, J.; Luo, Y.; Fu, W.; Zhou, L.; Wang, X.; Wang, Y.; Yang, Z.; Yao, X.; Ren, M.; et al. MicroRNA let-7f-5p regulates PI3K/AKT/COX2 signaling pathway in bacteria-induced pulmonary fibrosis via targeting of PIK3CA in forest musk deer. *Peer J.* **2022**, *10*, No. e14097.
(44) Chen, Y.; Li, X.; Li, Y.; Wu, Y.; Huang, G.; Wang, X.; Guo, S. Downregulation of microRNA-423−5p suppresses TGF-beta1-induced EMT by targeting FOXP4 in airway fibrosis. *Mol. Med. Rep* **2022**, *26* (1), DOI: 10.3892/mmr.2022.12758.
(45) Wu, M. M.; Wang, Q. M.; Huang, B. Y.; Mai, C. T.; Wang, C. L.; Wang, T. T.; Zhang, X. J. Dioscin ameliorates murine ulcerative colitis by regulating macrophage polarization. *Pharmacol. Res.* **2021**, *172*, No. 105796.
(46) *The Human Protein Atlas*. Available via the Internet at: www.proteinatlas.org/ENSG00000004468-CD38/tissue+cell+type (accessed Feb. 14, 2022).
(47) Paino, T.; Ocio, E. M.; Paiva, B.; San-Segundo, L.; Garayoa, M.; Gutierrez, N. C.; Sarasquete, M. E.; Pandiella, A.; Orfao, A.; San Miguel, J. F. CD20 positive cells are undetectable in the majority of multiple myeloma cell lines and are not associated with a cancer stem cell phenotype. *Haematologica* **2012**, *97* (7), 1110−1114.
(48) Han, D.; Xu, Y.; Peng, W. P.; Feng, F.; Wang, Z.; Gu, C.; Zhou, X. Citrus Alkaline Extracts Inhibit Senescence of A549 Cells to Alleviate Pulmonary Fibrosis via the beta-Catenin/P53 Pathway. *Med. Sci. Monit.* **2021**, *27*, No. e928547.
(49) Covarrubias, A. J.; Kale, A.; Perrone, R.; Lopez-Dominguez, J. A.; Pisco, A. O.; Kasler, H. G.; Schmidt, M. S.; Heckenbach, I.; Kwok, R.; Wiley, C. D.; et al. Senescent cells promote tissue NAD(+) decline during ageing via the activation of CD38(+) macrophages. *Nat. Metab.* **2020**, *2* (11), 1265−1283.
(50) Ashcroft, T.; Simpson, J. M.; Timbrell, V. Simple method of estimating severity of pulmonary fibrosis on a numerical scale. *J. Clin. Pathol.* **1988**, *41* (4), 467−470.
(51) Liu, X.; Liu, C.; Zheng, Z.; Chen, S.; Pang, X.; Xiang, X.; Tang, J.; Ren, E.; Chen, Y.; You, M.; et al. Vesicular Antibodies: A Bioactive Multifunctional Combination Platform for Targeted Therapeutic Delivery and Cancer Immunotherapy. *Adv. Mater.* **2019**, *31* (17), No. e1808294.
(52) Drent, E.; Themeli, M.; Poels, R.; de Jong-Korlaar, R.; Yuan, H.; de Bruijn, J.; Martens, A. C. M.; Zweegman, S.; van de Donk, N.; Groen, R. W. J.; et al. A Rational Strategy for Reducing On-Target Off-Tumor Effects of CD38-Chimeric Antigen Receptors by Affinity Optimization. *Mol. Ther.* **2017**, *25* (8), 1946−1958.
(53) Murphy, D. E.; de Jong, O. G.; Brouwer, M.; Wood, M. J.; Lavieu, G.; Schiffelers, R. M.; Vader, P. Extracellular vesicle-based therapeutics: natural versus engineered targeting and trafficking. *Exp Mol. Med.* **2019**, *51* (3), 1−12.
(54) Liang, Y.; Xu, X.; Xu, L.; Iqbal, Z.; Ouyang, K.; Zhang, H.; Wen, C.; Duan, L.; Xia, J. Chondrocyte-specific genomic editing enabled by hybrid exosomes for osteoarthritis treatment. *Theranostics* **2022**, *12* (11), 4866−4878.
(55) Hovhannisyan, L.; Riether, C.; Aebersold, D. M.; Medova, M.; Zimmer, Y. CAR T cell-based immunotherapy and radiation therapy: potential, promises and risks. *Mol. Cancer* **2023**, *22* (1), 82.
(56) Frankell, A. M.; Dietzen, M.; Al Bakir, M.; Lim, E. L.; Karasaki, T.; Ward, S.; Veeriah, S.; Colliver, E.; Huebner, A.; Bunkum, A.; et al. The evolution of lung cancer and impact of subclonal selection in TRACERx. *Nature* **2023**, *616* (7957), 525−533.
(57) Cho, S. J.; Stout-Delgado, H. W. Aging and Lung Disease. *Annu. Rev. Physiol.* **2020**, *82*, 433−459.
(58) Lei, Q.; Gao, F.; Liu, T.; Ren, W.; Chen, L.; Cao, Y.; Chen, W.; Guo, S.; Zhang, Q.; Chen, W.; et al. Extracellular vesicles deposit PCNA to rejuvenate aged bone marrow-derived mesenchymal stem cells and slow age-related degeneration. *Sci. Transl Med.* **2021**, *13* (578), DOI: 10.1126/scitranslmed.aaz8697.
(59) Xu, C.; Zhao, J.; Li, Q.; Hou, L.; Wang, Y.; Li, S.; Jiang, F.; Zhu, Z.; Tian, L. Exosomes derived from three-dimensional cultured human umbilical cord mesenchymal stem cells ameliorate pulmonary fibrosis in a mouse silicosis model. *Stem Cell Res. Ther.* **2020**, *11* (1), 503.
(60) Smyth, T.; Kullberg, M.; Malik, N.; Smith-Jones, P.; Graner, M. W.; Anchordoquy, T. J. Biodistribution and delivery efficiency of unmodified tumor-derived exosomes. *J. Controlled Release* **2015**, *199*, 145−155.
(61) Usman, W. M.; Pham, T. C.; Kwok, Y. Y.; Vu, L. T.; Ma, V.; Peng, B.; Chan, Y. S.; Wei, L.; Chin, S. M.; Azad, A.; et al. Efficient RNA drug delivery using red blood cell extracellular vesicles. *Nat. Commun.* **2018**, *9* (1), 2359.
(62) Lei, Q.; Liu, T.; Gao, F.; Xie, H.; Sun, L.; Zhao, A.; Ren, W.; Guo, H.; Zhang, L.; Wang, H.; et al. Microvesicles as Potential Biomarkers for the Identification of Senescence in Human Mesenchymal Stem Cells. *Theranostics* **2017**, *7* (10), 2673−2689.
(63) Puzar Dominkus, P.; Stenovec, M.; Sitar, S.; Lasic, E.; Zorec, R.; Plemenitas, A.; Zagar, E.; Kreft, M.; Lenassi, M. PKH26 labeling of extracellular vesicles: Characterization and cellular internalization of contaminating PKH26 nanoparticles. *Biochim. Biophys. Acta Biomembr.* **2018**, *1860* (6), 1350−1361.

https://doi.org/10.1021/acsnano.3c10547
ACS Nano 2024, 18, 7046−7063